

Study of selected mild steels for application in vacuum systems of future gravitational wave detectors

Carlo Scarcia,^{1, a)} Giuseppe Bregliozzi,¹ Paolo Chiggiato,¹ Alice Ingrid Michet,¹ Ana Teresa Perez Fontenla,¹ Martino Rimoldi,¹ Mauro Taborelli,¹ and Ivo Wevers¹
CERN

(Dated: 12 June 2024)

Next-generation gravitational wave detectors (GWDs) like the Cosmic Explorer and Einstein Telescope require extensive vacuum tubing, necessitating cost-effective materials. This study explores the viability of mild steel as an alternative to austenitic stainless steel for UHV beampipes, focusing on outgassing rates and surface chemistry after low-temperature bakeouts. Mild steels exhibit significantly lower hydrogen outgassing rates, below 10^{-14} mbar l s⁻¹ cm⁻² after bakeouts at 80°C for 48 hours. While water vapor is the primary residual gas after such low-temperature bakeouts, repeated treatments reduce its outgassing rate and modify surface conditions so that such benefit is preserved after at least six months of exposure to laboratory air. These findings position mild steel as an economical and efficient material for future GWD beampipes.

^{a)}RWTH Aachen, Institute III B; email address: carlo.scarcia@cern.ch

I. INTRODUCTION

Since the first recorded signals in 2015¹, the detection of gravitational waves has opened a new window of observation into the universe, contributing to a deeper understanding of cosmological and astronomical events. Gravitational wave detectors (GWD) employ ultra-sensitive laser interferometry to reveal space-time deformations, meticulously studying and attenuating all noise sources². One significant noise source is the residual gas present in the vacuum tubes of the interferometer. Pressures in the ultra-high vacuum (UHV) range are necessary to mitigate statistical fluctuations in the number of molecules within the volume traversed by the laser beam, thereby minimizing variations in the refractive index and photon phase shift. UHV conditions are designed to ensure that pressure-related noise remains at least an order of magnitude lower than the sum of all other sources of noise, including seismic, thermal, quantum, and Newtonian effects.

While current GWDs (such as LIGO³, Virgo⁴, and KAGRA⁵) continue to provide valuable insights through successive enhancements, their capabilities are limited, offering only a partial glimpse of the gravitational universe. To expand the potential discovery landscape, a third generation (3G) of GWDs is being proposed, notably the Cosmic Explorer (CE) in the USA and the Einstein Telescope (ET) in Europe. The CE proposal foresees two right-angle interferometers at distinct locations, featuring arms that are 10 times longer than those of LIGO. This configuration necessitates approximately 160 km of vacuum tubing with an internal diameter of 1.2 meters⁶. The ET project, on the other hand, will consist of six interferometers underground within a triangular tunnel measuring 10 km on each side. This setup requires approximately 120 km of vacuum piping with an internal diameter of 1 meter⁷.

The remarkable size of the vacuum system and its significant influence on the projected total cost call for revised designs, fabrication methods, and materials, as a mere scale-up of the second-generation GW detectors would be economically prohibitive. In this perspective, it is crucial to choose a material that ensures ultrahigh vacuum performance while also offering a lower cost than the austenitic stainless steels currently in existing gravitational wave observatories⁸.

A potential alternative to austenitic stainless steel for manufacturing UHV chambers could be low-carbon steels^{6,9}. Commercially known as mild steel, it is widely used as a structural material due to its affordability and excellent mechanical properties. In vacuum technology, mild steel is commonly employed in systems operating within pressure ranges above 10^{-6} mbar^{10,11}. However, its broad adoption in a wider spectrum of applications is limited by several factors. Firstly, it is

prone to corrosion¹², and its production process is primarily tailored for structural applications, often neglecting the surface finishing. Furthermore, its ferromagnetic properties pose a considerable limitation to application in particle accelerators and surface science equipment. Additionally, mild steel exhibits a significant CO outgassing rate¹¹ when exposed to high temperatures due to the high C content. In the past, only a few authors have described the outgassing rate of mild steels, resulting in discouraging results when compared to austenitic stainless steels. The water outgassing rates reported in the literature and textbooks often exhibit significant variability, sometimes differing by as much as three orders of magnitude^{13,14}. Furthermore, the lack of detailed information about the grade, surface conditions, cleaning procedures, or thermal treatments in these reports complicates the ability to conduct a thorough comparison. Scarce information could also be found for the hydrogen outgassing rate after bakeout. Indeed, the most complete results were reported for a C15E steel (S15C, according to JIS standard) after a bakeout at 300°C for 3h¹⁵, where mild steel showed values one order of magnitude higher than a 304L austenitic stainless steel baked at 150°C for 24h¹⁶. Despite these discouraging results, a recent study has shown that mild steels could still be developed and applied in UHV environments^{17,18}. Indeed, using commercially available alloys, Park et al. measured a H₂ outgassing rate from mild steel that was 10 to 50 times lower than austenitic stainless steel subjected to a similar bakeout procedure (i.e., 150°C for 48h). The same work gave a qualitative picture of the vacuum performance of low-carbon steels; however, the information is limited only to H₂ and H₂O outgassing rates. Other interesting results were recently presented¹⁹.

This study aims to evaluate mild steel as a potential material for vacuum tubes 3G GWD. We measured the outgassing rates of well-defined mild steels for the typical gas species found in UHV environments, including H₂, H₂O, CH₄, CO, and CO₂. To ensure cost-effectiveness, we utilized only readily available off-the-shelf products and assessed the impact of low-temperature bakeouts on outgassing rates. Temperature Programmed Desorption (TPD) measurements were employed to estimate the H₂ content in the analysed samples. Furthermore, we conducted additional X-ray Photoelectron Spectroscopy (XPS) measurements to monitor the surface condition of the samples after heating at various temperatures.

II. EXPERIMENTAL APPARATUS AND METHODS

A. THROUGHPUT METHOD

The outgassing rates of unbaked samples were measured using the throughput method^{20,21}. The measurement consisted of monitoring as a function of pumping time, the pressure in the test dome divided into two sides by the interposition of an orifice. On one side, the sample was placed either as a set of specimens inserted in a sample holder or as a connected vacuum chamber. On the other side of the orifice, a turbomolecular pumping group was connected by means of an all-metal right-angle valve (see Fig.1). The outgassing rate of the sample per unit of geometrical surface area tested is calculated as:

$$q_i = \frac{[C_i \cdot (P_1 - P_{1,BGD}) - (P_2 - P_{2,BGD})]}{A_{sample}} \left[\frac{mbar \cdot l}{s \cdot cm^2} \right] \quad (1)$$

where C_i is the conductance of the orifice for the gas of interest (index 'i'); P indicates the measured pressures in the sample side, with index '1', and pump side, with index '2'. The index 'BGD' stands for background, and it indicates the pressures recorded at the same pumping time without the sample installed in the system. The subtraction of background pressures is required to remove the contribution of the austenitic stainless steel test dome and gauges to the total outgassing rate. The geometrical surface area of the sample is indicated as A_{sample} . During the measurements, the temperature was stabilised at $21 \pm 2^\circ\text{C}$. The orifice had a diameter of 0.8 cm, which results in $C_{H_2O} = 7.4 \text{ ls}^{-1}$. The test dome had a diameter of 10 cm; it was connected to the sample holder or the sample chamber by a DN100 CF flange. The pressure measurement was performed by cold cathode gauges (Pfeiffer IKR070, estimated accuracy $\pm 30\%$). The specific outgassing rate was monitored for approximately 100 h of pumping. The background measurements were repeated every time a new steel grade was tested.

B. COUPLED ACCUMULATION-THROUGHPUT METHOD

The coupled accumulation-throughput method²¹ was employed to measure the post-bakeout outgassing rate of the samples (see Fig.2). The all-metal measurement system consisted of a throughput system connected to the sample holder via a variable leak valve (VLV). Alternatively, the sample was the vacuum vessel to be measured connected directly to the VLV. Pumpdown, leak detection, and bakeout procedures were routinely conducted with the VLV left fully open.

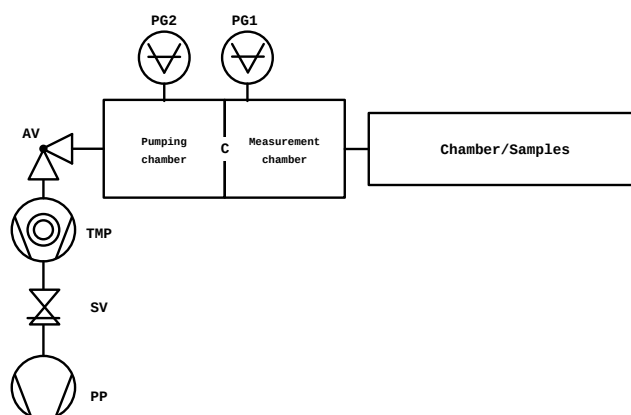


FIG. 1: Schematic of the throughput system. TMP: turbomolecular pump; SV: electromagnetic safety valve; PP: primary pump; AV: right angle valve; C: orifice conductance; PG1 and PG2: pressure gauge 1 and 2.

However, when performing an outgassing measurement, the VLV was fully closed, allowing the released gas to accumulate within the inner volume of the sample holder for a specified accumulation period. Subsequently, the VLV was gradually opened. The gas escaping from the sample holder was then detected using a residual gas analyser (RGA, Pfeiffer QMA 125) employing multiple ion detection (MID) and a Bayard-Alper gauge (BA, SVT305 CERN²², accuracy $\pm 10\%$). The detection terminated when the pressure reached a reasonably stable value, and the VLV was closed for a new accumulation. A TMP group ensured the required pumping speed during pump-down and bakeout. To attain H_2 pressures in the low 10^{-11} mbar range, a Sputter Ion Pump (SIP) and a Titanium Sublimation Pump (TSP) were employed during the system operation. A 0.8 cm diameter orifice separated the pumping chamber from the measurement chamber where the RGA and BA gauge were installed. To avoid drift in the sensitivities, the RGA was regularly calibrated in situ against the BA gauge²³. Unlike other accumulation techniques, this method provides outgassing rate values for specific gas species, assuming their partial pressure during accumulation varies linearly with time. This condition is met for gases with negligible sticking probabilities on sample holder surfaces, typically observed with hydrogen and methane. However, water vapor, prone to re-adsorption on sample surfaces, violates this linearity. H_2O molecules readsorb on the surfaces of the sample holder to attain equilibrium between accumulated gas and surface coverage. An advantage of this system is the absence of indirect gas pumping or cracking since no ion gauges are installed in the accumulation volume. Measurements are repeated for different accumulation

times to confirm the measurement's linearity and increase its accuracy. The accumulated quantity of gas Q_{acc} , in the time interval t_a , is calculated using Eq.2.

$$Q_{acc} = S_c \cdot \int_{t_a}^{t_a + \Delta t} I_{RGA}(\tau) \times \alpha_{RGA} d(\tau) \left[\frac{\text{mbar} \cdot l}{s} \right] \quad (2)$$

where Δt is the actual duration of the RGA recording, I_{RGA} is the ion current read by the RGA, α_{RGA} is the calibration factor relating current and pressure for the gas of interest, and S_c denotes the effective pumping speed at the level of the RGA. Assuming linearity, the specific outgassing rate q of the sample is computed as:

$$q_{acc} = \frac{Q_{acc} - Q_{BGD}}{A_s} \left[\frac{\text{mbar} \cdot l}{s \cdot \text{cm}^2} \right] \quad (3)$$

Q_{BGD} is the accumulated gas quantity measured without samples (background) after undergoing an identical bakeout cycle. If the sample is a vacuum vessel, Q_{BGD} accounts for the gas released from the VLV and flanges used for vessel closure. The sample's geometrical surface area was maximized to increase system sensitivity. To minimize other gas sources, all components that constitute the throughput system and sample holder were vacuum fired for 2 h at 950°C^{21} prior to installation. The VLV was dismantled, and each stainless steel sub-component underwent the same vacuum firing treatment.

The sample holder was baked at 80°C and 150°C for 48 h. The throughput system and VLV underwent bakeout at temperatures ranging from 200°C to 350°C . The accumulation measurements started when the samples were at room temperature ($21 \pm 2^\circ\text{C}$), 24 h after the end of the bakeout cycle.

C. TEMPERATURE PROGRAMMED DESORPTION

Temperature Programmed Desorption (TPD) measurements were conducted to ascertain the diffusible hydrogen content in the mild steel samples. The TPD analysis was carried out using a commercial TPD workstation²⁴. The system consisted of a testing chamber and a load-lock chamber, which were separated by a manual gate valve (GV). This GV maintained a UHV environment in the testing chamber, with a base pressure of approximately 1.5×10^{-9} mbar, while preserving the high vacuum conditions in the load-lock chamber, with a base pressure of about 1.5×10^{-7} mbar. This setup obviated the need for a bakeout of the test chamber upon inserting a new sample. Cold cathode gauges were installed in both chambers to monitor pressure levels. Additionally,

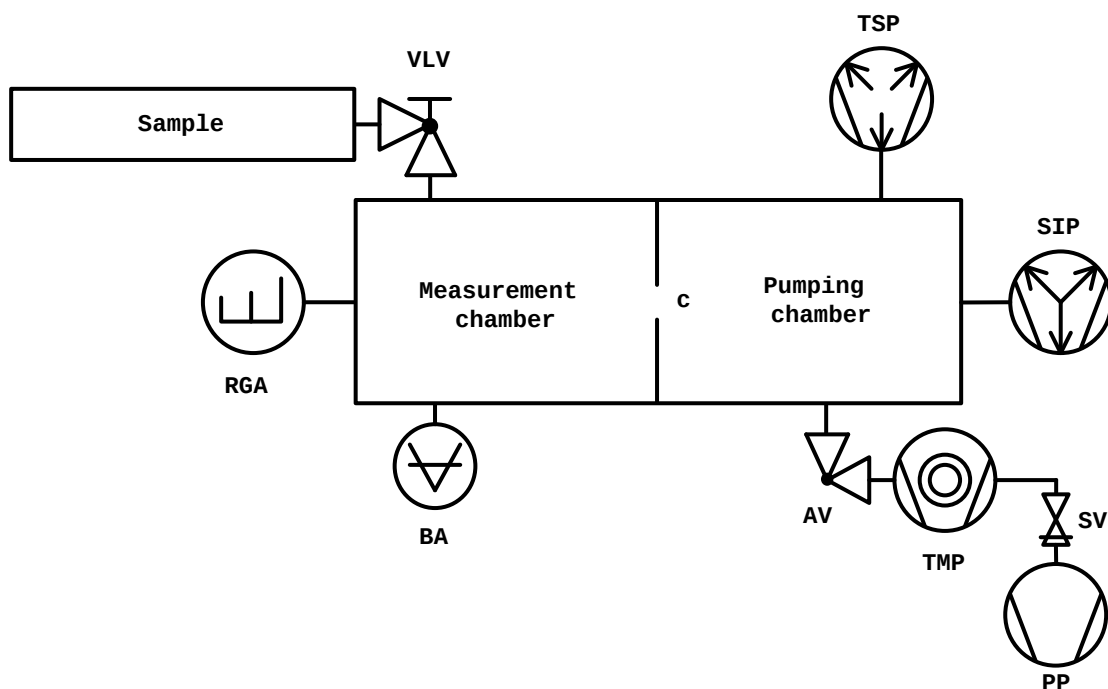


FIG. 2: Schematic of the coupled accumulation – throughput system. TMP: turbomolecular pump; SV: electromagnetic safety valve; PP: primary pump; AV: right angle valve; C: orifice conductance; BA: Bayard-Alpert gauge; SIP: sputter ion pump; TSP: Ti sublimation pump; RGA: residual gas analyser.

the testing chamber featured an RGA (Hiden 3F PIC) directly facing the sample to monitor gas evolution during measurements. The samples, each having a surface area of 2 cm² and thickness varying from 0.069 to 0.4 cm, underwent heating from 25°C to 940°C at a ramp rate of 5°C/min. To ensure measurement reproducibility, the background was re-measured after every ten samples. The accuracy of quantitative measurements was verified through regular in-situ calibration of the RGA. Hydrogen concentration calculation relied on sample weight, measured with a weight scale with a sensitivity of ±0.1 mg.

D. X-RAY PHOTOELECTRON SPECTROSCOPY

The surface chemical composition and chemical states were characterized by X-ray Photoelectron Spectroscopy (XPS) using a commercially available UHV system (measurement cham-

ber base pressure $<3 \times 10^{-10}$ mbar) from SPECS Surface Nano Analysis GmbH equipped with a monochromatized Al $K\alpha$ source. The energy scale of the electron analyser was calibrated on the Au $4f_{7/2}$ and Cu $2p_{3/2}$ lines of sputter-cleaned samples. The 1 cm² samples were measured at normal emission at room temperature. XPS spectra were taken after in-situ thermal treatment at 80°C and 150°C (heating ramp of 3°C/min, steady state of 17 h) to investigate the surface evolution during bakeout.

E. E. ULTIMATE PRESSURE AFTER LOW-TEMPERATURE BAKEOUT

Ultimate pressures after low-temperature bakeouts were investigated using a dedicated system. The sample, a mild steel vacuum chamber, underwent a series of consecutive bakeouts at 80°C, each lasting 48 h, until the system's pressure limit was attained. The ultimate pressure at room temperature ($21 \pm 2^\circ\text{C}$) was measured 24 h after the end of each bakeout, without intermediate air venting.

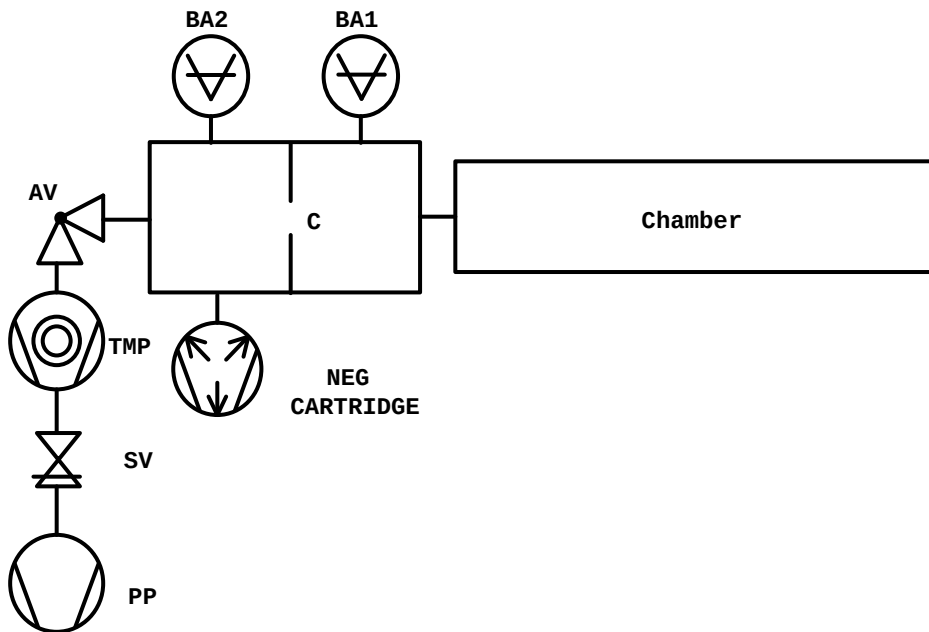


FIG. 3: Schematic of the ultimate pressure system. NEG: Non Evaporable Getter.

All the stainless-steel components of the system (see Fig.3) were vacuum fired at 950°C for 2h

to reduce their hydrogen outgassing rate. The sample was pumped through an orifice (C) with a diameter of 1 cm (9.2 ls^{-1} for N_2) by a Non-Evaporable Getter (NEG) cartridge that provided a 2000 ls^{-1} nominal pumping speed for H_2 . A TMP group (effective pumping speed 120 ls^{-1} for N_2) was also installed to ensure pumping during bakeouts and to remove species that are not adsorbed by the NEG pump, i.e. rare gases and methane. The pressure measurements across the orifice were carried out by calibrated BA gauges (SVT305 CERN, accuracy $\pm 10\%$). The mild steel sample was connected to the test system by a DN100 CF AISI 316LN vacuum fired flange welded at the extremity. During the bakeout of the sample, the rest of the system was baked at temperatures in the range 200°C to 350°C , keeping the vacuum gauges always at the highest temperature. If the sample is not installed, the achieved pressure after bakeout in the dome where BA2 is installed is about 2×10^{-12} mbar (N_2 equivalent).

III. MATERIAL SELECTION AND SAMPLE PREPARATION

Mild steel off-the-shelf blocks, sheets/plates, and tubes were provided by different suppliers. They were compared with AISI 304L stainless steel available at CERN and meant for UHV application. The characteristics of the selected steels are listed in Tab. I. Samples for the analysis were cut from blocks and plates to the required dimensions using a bench shear. Before sample cutting, the blocks were milled on the external surfaces to remove the surface damaged layer. In the case of tubes, DN100 CF AISI 316LN flanges were welded at both ends after cutting samples for TPD and XPS analysis. DN100 CF AISI 316LN blank flanges were also prepared to perform pump-down, accumulation and ultimate pressure measurements. All flanges prior to welding were vacuum fired at 950°C for 2 h. The part of the blank flanges exposed to the vacuum was thinned to increase the hydrogen degassing efficiency of vacuum firing²⁵. Mild steel samples were then cleaned in a solvent bath (DowcleanTM 1601 for tubes and TopkleanTM MC 20A for the other samples) by immersion, ultrasonic agitation, and, finally, dried in an air furnace at 60°C for 30 min before being tested. The AISI 304L samples, instead, were cleaned following the CERN UHV standard procedure²⁶ that implies the use of a detergent bath (NGL 17.40 spec. ALU III), rinsing with de-mineralized water, and drying in an air furnace at 60°C for 10-60 min.

TABLE I: Chemical composition (wt.%) of the selected steels with the corresponding manufacturing process (MP), heat treatment (HT), and shape. AISI 304L chemical composition values are to be intended as the maximum content allowed²⁷. HR: Hot rolled, CR: Cold rolled, AP: Acid pickled, ERW: Electric Resistance Welded.

	S355J+AR	S355J2+N	FB580	ULC-IF	ARMCO (grade 4)	S355J2H	P355N	AISI 304L
MP	HR	HR + Forged	HR	CR	CR	HR+ERW	HR+AP+ERW	CR
HT	None	Normalization	None	None	None	None	Normalization	Solution annealed
Shape	Block	Block	Sheet	Sheet	Sheet	Tube	Tube	Plates
C	0.14	0.14	0.086	0.013	0.002	0.20	0.19	0.03
Mn	1.46	1.46	1.35	0.099	0.04	1.32	1.31	2.0
Si	0.20	0.20	0.045	0.005	0.003	0.17	0.16	1.0
Cu	0.06	0.06	0.009	0.008	0.008	0.08	0.13	-
Al	0.03	0.03	0.038	0.049	0.002	0.03	0.03	-
S	0.01	0.01	0.0012	0.0094	0.0018	0.01	0.0001	-
P	0.01	0.01	0.0108	0.0093	0.004	0.01	0.01	0.03
N	0.01	0.01	-	-	-	0.004	0.01	0.02
Cr	-	-	0.025	0.023	0.014	-	-	17-20
Ni	-	-	0.01	0.011	0.015	-	-	10-12.5
Fe	Remainder	Remainder	Remainder	Remainder	Remainder	Remainder	Remainder	Remainder

IV. RESULTS AND DISCUSSION

A. Water vapor outgassing rate

The measured pumpdown curves, representing the water vapor specific outgassing rate as a function of pumping time, are shown in Figure 4. The specific outgassing rates recorded after 10 h of pumping are summarized in Table II.

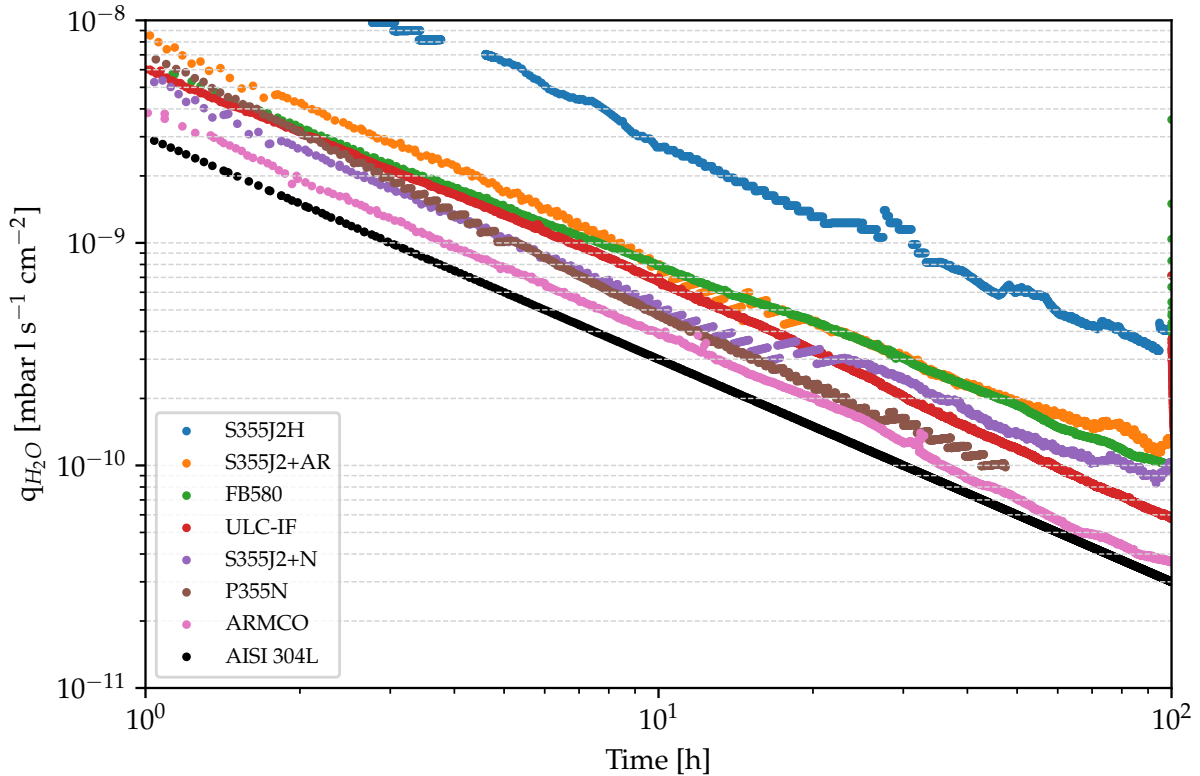


FIG. 4: Pumpdown curves at $21 \pm 2^\circ\text{C}$; the specific outgassing rate is plotted as a function of the pumping time. The background value is subtracted. The 304L curve is calculated from an empirical relationship generally applied at CERN for austenitic stainless steels applied in UHV²¹.

As shown in Figure 4, the pumpdown values of all mild steel samples are reasonably fitted by inverse power laws in which the exponents of time are around -1. This is the typical behaviour of metal surfaces discussed and interpreted by some authors^{28,29}. In terms of quantitative data, there is a significant dispersion ranging from 1.2 to 10 times higher values than AISI 304L. The lowest specific outgassing rates are reported for samples cut from blocks, while the highest ones are recorded for the S355J2H pipe. Scanning Electron Microscope (SEM) micrographs were

taken for the S355J2H surface (see Fig.6). The S355J2H surface morphology appeared rough, characterized by cracks and small pores, and covered by particulates of a few μm size. Further, a SEM-FIB (Focus Ion Beam) cross-section (Fig.7) displays a $10\ \mu\text{m}$ thick oxide layer covering the S355J2H surface. The oxide exhibits significant cracks, partial detachment from the substrate, and pores that appear open to the surface, features not seen for the other mild steel samples (see Figs. 8 to 13 for comparison). The poor surface condition may be responsible for the high rate of water outgassing.

TABLE II: Water vapor specific outgassing rates measured at $21\pm 2^\circ\text{C}$. **value estimated from the inverse power law fit at 10 h. Background removed.

Steel	Tested samples [cm ²]	q_{10h} [mbar l s ⁻¹ cm ⁻²]	$q_0 t_h^{-a}$
S355J2H	8821	2.7×10^{-9}	$2.6 \times 10^{-8} t_h^{-0.96}$
S355J2+AR	3536	8.1×10^{-10}	$8.0 \times 10^{-9} t_h^{-0.99}$
FB580	5956	7.9×10^{-10}	$6.9 \times 10^{-9} t_h^{-0.95}$
ULC-IF	6092	6.7×10^{-10}	$6.2 \times 10^{-9} t_h^{-0.97}$
S355J2+N	5780	4.9×10^{-10}	$5.1 \times 10^{-9} t_h^{-1.02}$
P355N	5938	4.7×10^{-10}	$6.8 \times 10^{-9} t_h^{-1.16}$
ARMCO	6050	3.9×10^{-10}	$4.0 \times 10^{-9} t_h^{-1.01}$
AISI 304L	-	$3.0 \times 10^{-10**}$	-

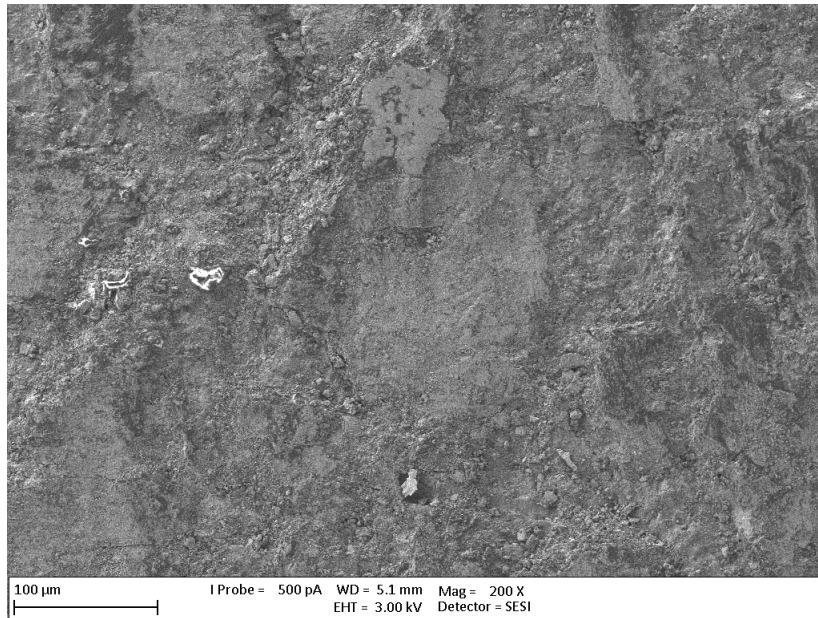


FIG. 5: SEM micrograph of the surface of the S355J2H sample.

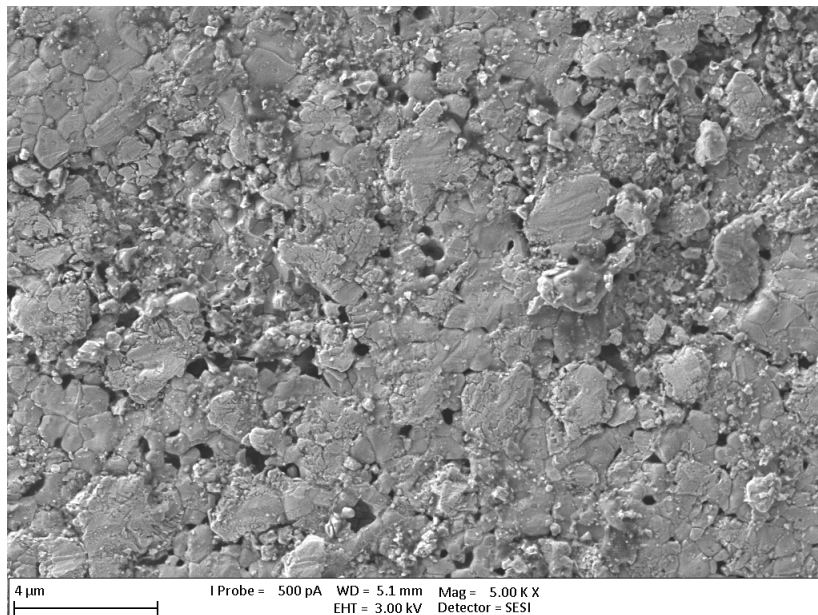


FIG. 6: SEM micrograph of the surface of the S355J2H sample. Pores and flakes are covering the surface.

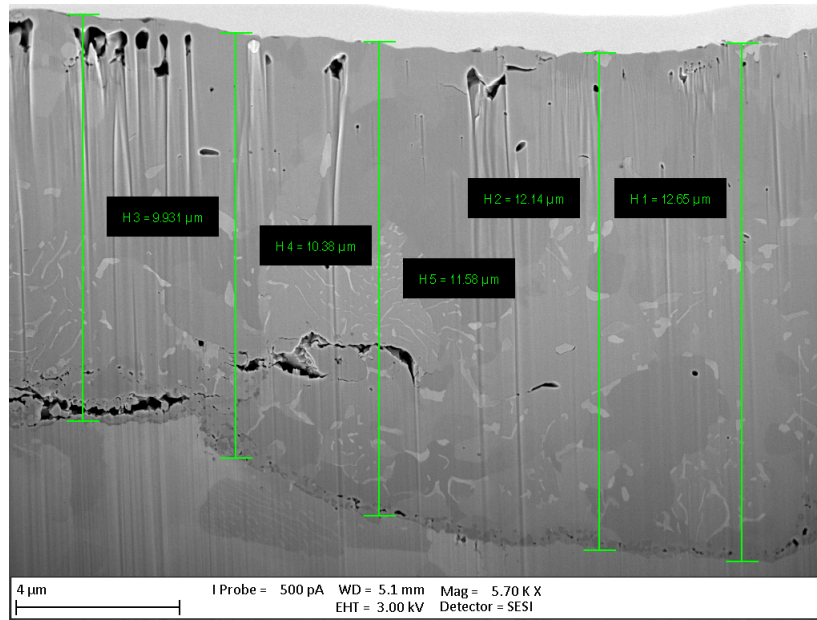


FIG. 7: SEM-FIB cross-section micrograph of the S355J2H surface. The thickness of the oxide layer is highlighted by bars in five different positions.

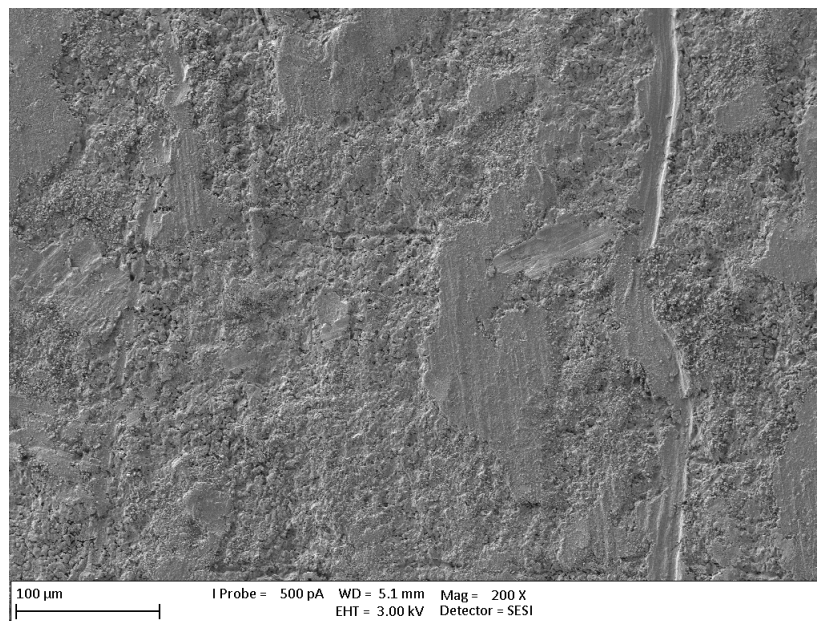


FIG. 8: SEM micrograph of the surface of the P355N sample.

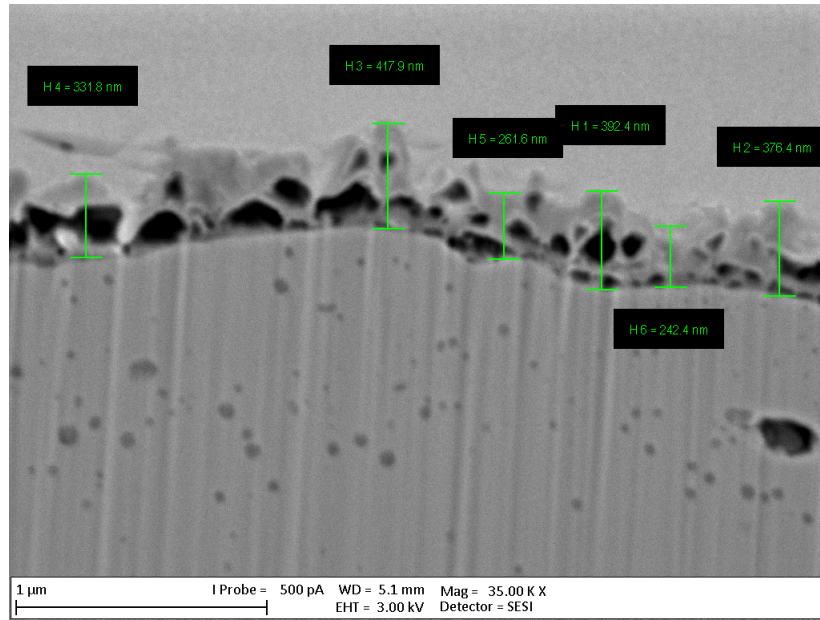


FIG. 9: SEM-FIB cross-section micrograph of the P355N surface highlighting an oxidated spot. The thickness of the oxide layer is highlighted by bars in six different positions.

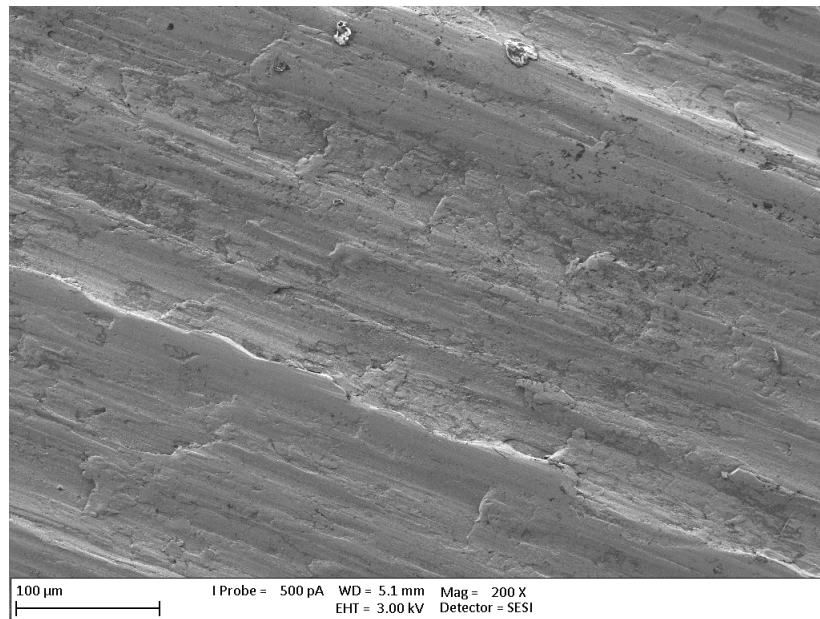


FIG. 10: SEM micrograph of the surface of the S355J2+AR sample.

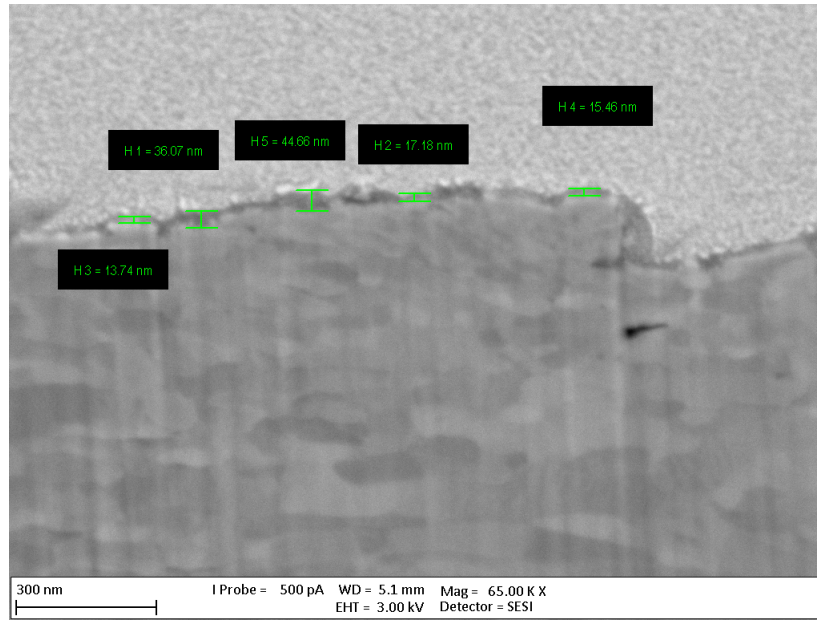


FIG. 11: SEM-FIB cross-section micrograph of the S355J2+AR surface highlighting an oxidated spot. The thickness of the oxide layer is highlighted by bars in five different positions.

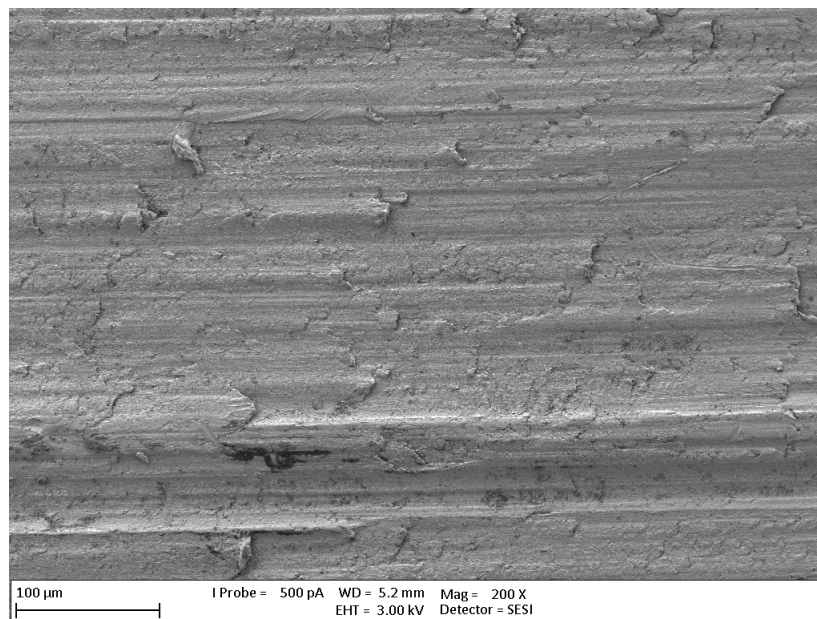


FIG. 12: SEM micrograph of the surface of the S355J2+N sample.

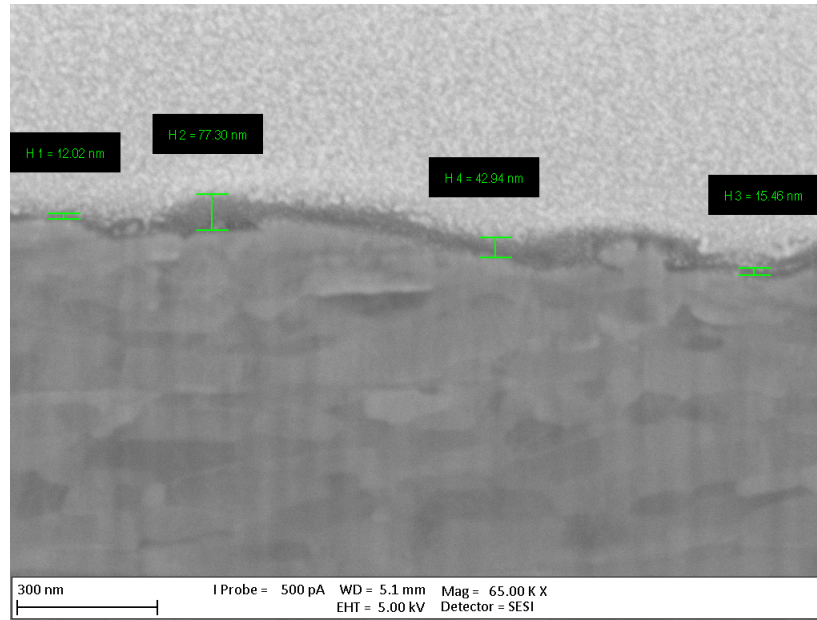


FIG. 13: SEM-FIB cross-section micrograph of the S355J2+N surface highlighting an oxidated spot. The thickness of the oxide layer is highlighted by bars in four different positions.

B. X-Ray Photoelectron Spectroscopy

The surface chemical composition of the steel samples, investigated by X-ray Photoelectron Spectroscopy (XPS), revealed C, O, and Fe as major constituents, along with a minor content of N, P, Si, and other metals. The evolution of the samples' surface was also investigated after in situ thermal treatments at 80°C and 150°C.

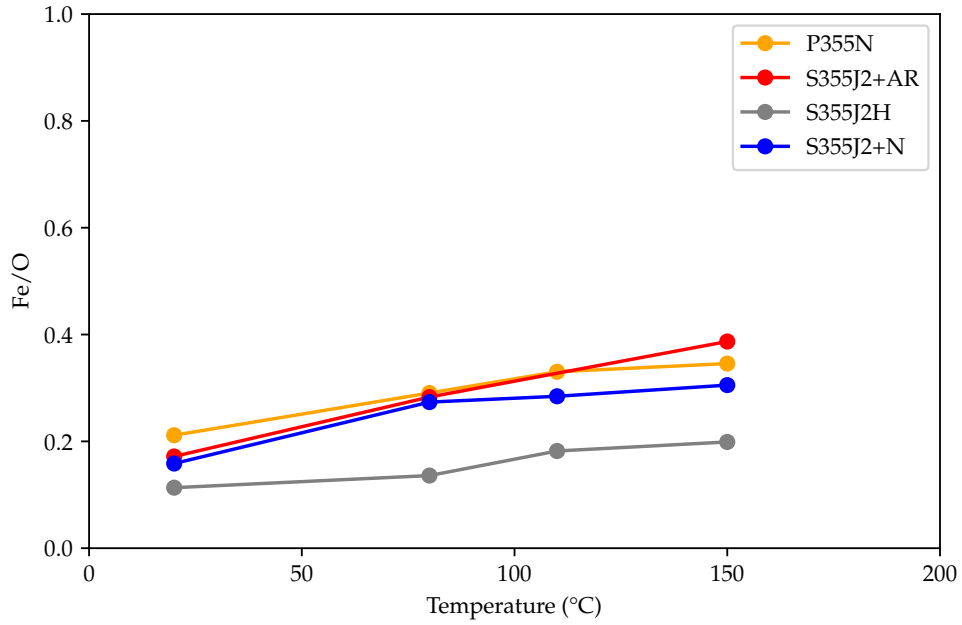
The elemental composition, analysed as the ratios between the three major components (C, O, and Fe) and visualized as Fe/C and Fe/O (Fig. 14), indicated, as a general trend, a progressive increase with the temperature of the relative surface iron content. Over the range of tested temperatures, the S355J2H samples demonstrated a lower relative surface iron content, whereas the other samples had relatively similar results to each other.

The detailed Fe 2p spectra probed the evolution of the surface oxides and hydroxides upon heating. At room temperature, the Fe 2p_{3/2} line was found in all samples at binding energies between 711.0 and 711.2 eV, indicating a Fe(III) oxide-hydroxide species (Fe(O)OH)^{30,31}. After prolonged heating at 80°C, a shift to lower binding energies was observed (approximately 710.7–710.8 eV) as a result of a surface rearrangement possibly consistent with a dehydration/dehydroxylation process. Concomitantly, Fe(II) satellites – broad features centred at 715 eV – became apparent and supported the occurrence of Fe(II) species in the surface layer probed by XPS. An increase in the thermal treatment temperature (up to 150°C) did not induce any further transformations on the structural steels (an example in Fig. 15a). On the other hand, above 80°C, the Fe2p lines of P355N further evolved, progressively shifting to lower binding energies (Fig. 15b). At 150°C (Fig. 16a), the P355N steels contained, with respect to the structural steels, a higher fraction of Fe species in oxidation state II, as demonstrated by the region of binding energies centred between 709 and 708.5 eV, characteristic of the Fe₃O₄ and FeO compounds^{30,31}

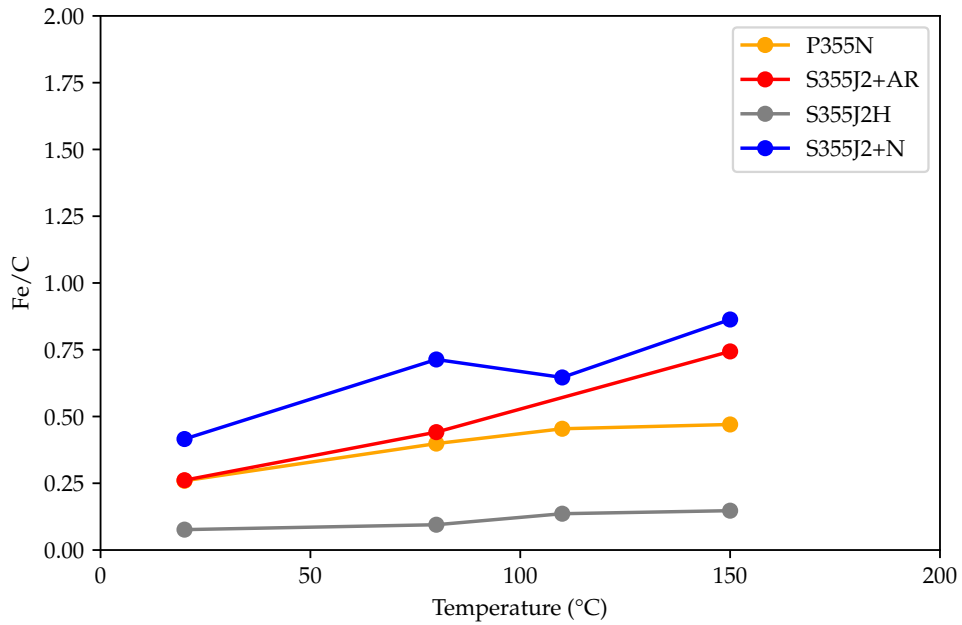
Moreover, Fe(0) (feature at ca. 706.7 eV) was observed in each sample, indicating a thin oxide layer of few nanometres, except for S355J2H that had, instead, a thicker surface oxide –as also probed by SEM (see Fig. 7).

The nature of the surface oxide species was also evaluated by O 1s XPS: two components, detected at 532 and 530 eV, were assigned to hydroxides (Fe–OH, terminal or bridging) and bulk oxides (O–Fe–O), respectively^{30,31} (Fig. 16b). Structural steels consisted of a higher relative fraction of hydroxides, differently from the P355N steel that instead had a higher bulk oxides component. It is worth mentioning that a broad O1s component at 533-534 eV, attributed to adsorbed water^{30,31},

was found in the room temperature spectra of the S355J2H, S355J2+N, and P355N steels, with the larger contribution seen in the former. The occurrence of adsorbed water has to be linked to high water outgassing rates; similarly, the high amount of surface hydroxides should indicate a material more prone to physisorb and chemisorb water. These arguments are supported by the higher outgassing value measured for S355JH2, with the presence of adsorbed water, low Fe/O ratio (Fig. 14a) and Fe 2p line shifted toward the hydroxide region (Fig. 16).

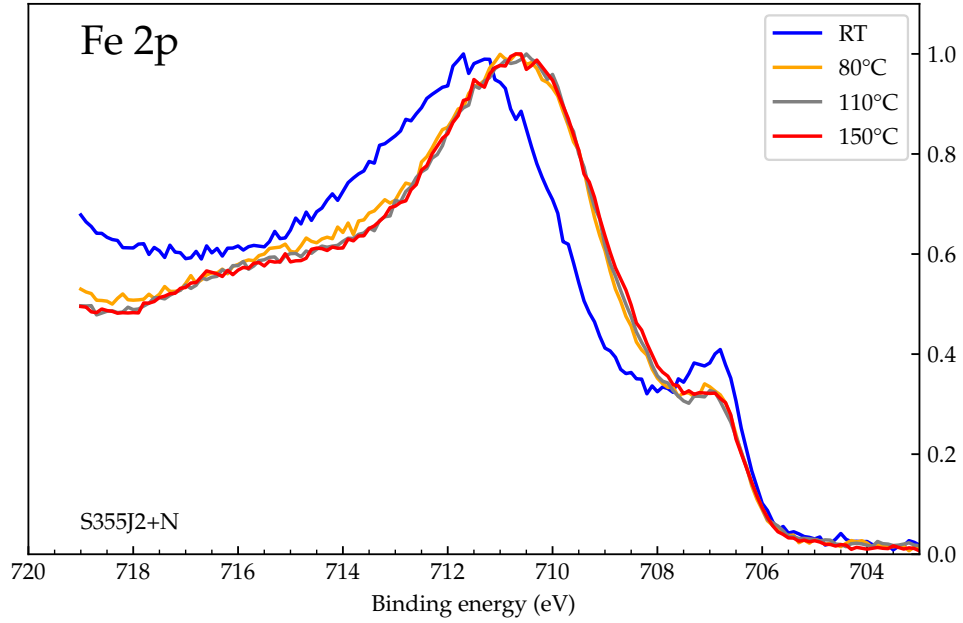


(a)

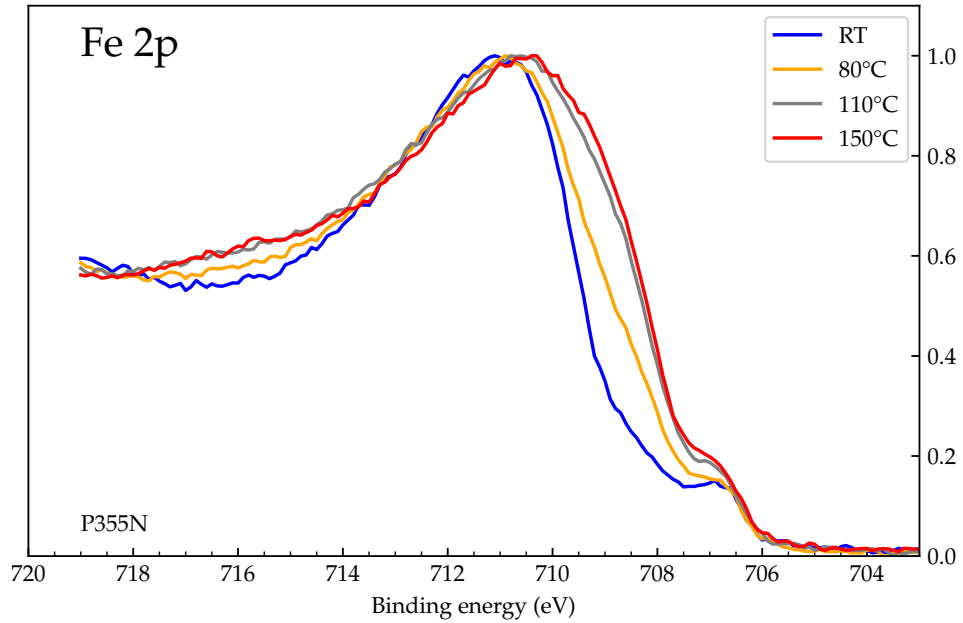


(b)

FIG. 14: Elemental composition as Fe/O and Fe/C ratios at RT, and after in-situ thermal treatments at 80°C, 110°C, and 150°C.

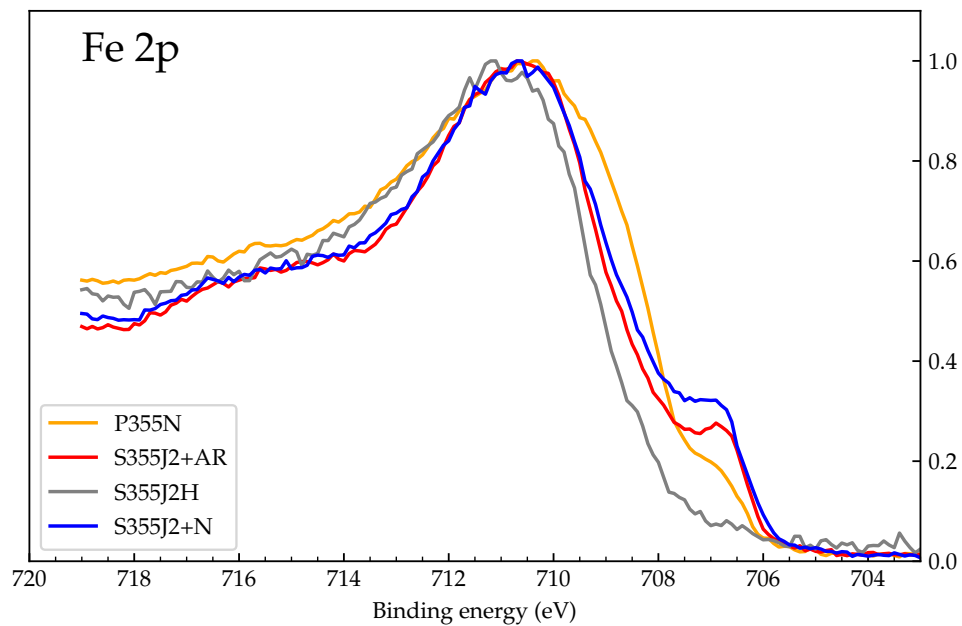


(a)

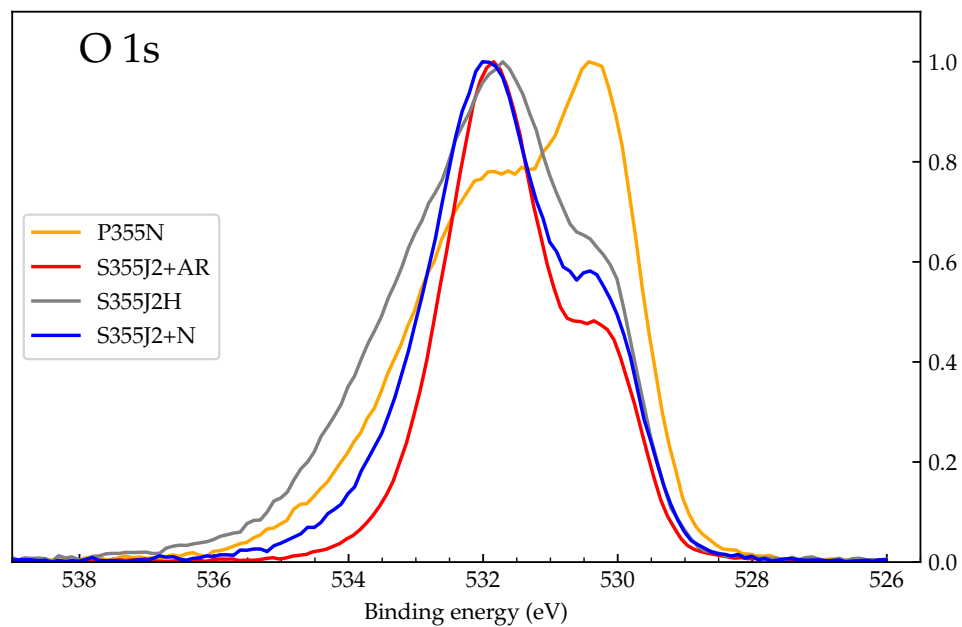


(b)

FIG. 15: Evolution of the Fe $2p_{3/2}$ XP spectra between RT and 150°C of two selected samples: (a) S355J2+N and (b) P355N.



(a)



(b)

FIG. 16: (a) Fe 2p_{3/2} and (b) O 1s XP spectra of the steel samples after thermal treatment at 150°C.

C. TEMPERATURE PROGRAMMED DESORPTION

The H₂ thermal desorption spectra, with the background signal removed, are shown in Figs. 17 to 19. As the thicknesses of the mild steel samples were not the same, the H₂ desorption spectra are represented normalised to the sample's weight. This choice can be argued. However, it is justified by the results reported hereafter. All raw data were smoothed for better visualization through a Savitzky-Golay filter³² implemented in Python.

The signal obtained with AISI 304L samples can be fitted by a Fickian diffusion model that matches the broad peak with a maximum at 615°C (see Fig. 17). The obtained diffusion energy is 0.52 ± 0.06 eV, i.e. a typical value for austenitic stainless steels^{33–35}.

Among the flat mild steel samples (see Fig. 18), we can identify a common peak/shoulder around 400°C–440°C. For the S355J2+AR, S355J2+N, ULC-IF, and FB580 samples, an additional concomitant peak/shoulder is observed between 520°C and 580°C. The common presence of a shoulder for the signals of S355J2+AR, S355J2+N, and FB580 is shown again around 780°C.

Very distinctive and different from the flat samples and from the P355N samples, the latter characterised by a small peak around 270°C and a relatively flat profile, is the H₂ desorption profile of the S355J2H samples (see Fig. 19). The desorption signal shows two small shoulders at 270°C and 380°C and a prominent and narrow peak at 530°C. Contrary to all the other types of samples, the signal after the peak starts a descending slope around 740°C before ramping up again at 780°C. To identify the origin of the high peak at 530°C, samples of S355J2H taken from the same delivery batch were immersed in an HCl solution for 2 min to remove the thick oxide layer. Once etched, the samples show a significantly lower desorption signal (Fig. 20). The desorption profile is characterized by a sharp peak at 170°C and a wide peak/shoulder at around 500°C.

The H₂ concentration in the measured samples is calculated by integrating the TPD signal up to 850°C and assuming uniform initial distribution in the volume of the samples. The results of the calculation are reported in Table III. The selection of the integration range is arbitrary, justified by the observation that hydrogen released at temperatures above 850°C is tightly bound, rendering it non-diffusible within the temperature range relevant to GWD. As shown in Fig. 20, a significant quantity of hydrogen can be attributed to the oxide layer. Consequently, the calculated bulk concentrations have to be considered upper limits.

The calculated hydrogen concentration in AISI 304L samples is 9.6 to 75 times higher than that evaluated for mild steel samples, the latter showing H contents always below 8 atomic ppm.

As expected from their body-centred cubic structure, the mild steel samples have a much lower hydrogen concentration than AISI 304L, which is face-centred cubic austenite. The different thicknesses and geometries of the tested samples do not allow a direct one-to-one comparison between the samples of mild steel; however, some general observations can be drawn. Given the shape of the peaks of the H₂ desorption profile of the mild steels, it appears that they are primarily influenced by the de-trapping of hydrogen from grain boundaries, lattice defects, carbides, and precipitates rather than Fickian bulk diffusion typical of the austenitic microstructure^{36–38}. Moreover, the shapes and intensities of the H₂ peaks are significantly influenced by the presence of thick iron oxides and hydroxides covering the samples. As can be seen from the etching of the S355J2H samples, hydrogen trapped in the oxide layers accounted for almost two-thirds of the total quantity of released hydrogen.

As depicted in Fig. 21 and Fig. 22, when heating the S355J2+N and S355J2+AR samples within the temperature range of 100°C to 450°C, a correlation becomes apparent between the peaks or shoulders of H₂ and those of CH₄, H₂O, CO, and CO₂. In this temperature range, water vapour is the leading gas; this result aligns with the XPS measurements (see Section IV B) that indicate significant dehydration and dehydroxylation already taking place during a temperature plateau at 80°C. Additionally, an intriguing overlap of peaks or shoulders of H₂, CO, and CO₂ is observed between temperatures of 500°C and 590°C. This latter temperature range coincides with the onset of Wustite (FeO) formation through the reduction of Hematite (Fe₂O₃) and Magnetite (Fe₃O₄)³⁹. The shoulders observed between 700°C and 800°C in the hydrogen desorption profile may potentially correspond to phase transformations within the steel samples, specifically from α -Fe + Fe₃C to α -Fe + γ -Fe. Similarly, the steeper shoulders observed between 800°C and 900°C could be attributed to a phase transformation from α -Fe + γ -Fe to γ -Fe⁴⁰. The simultaneous increase in CO desorption further supports these observations.

TABLE III: Hydrogen concentration obtained by integrating the TPD spectra up to 850°C. The values reported are the average of at least three samples from the same batch. The background of the TPD system is removed. To convert ppm at. to ppm wt. multiply by 55.85 (molecular weight of iron).

Steel	H content [ppm at.]	Thickness [cm]
AISI 304 (as received)	75	0.3
S355J2H	7.8	0.4
ULC-IF	3.7	0.69
FB580	2.8	2.1
S355J2H etched	2.7	0.4
S355J2+AR	2.0	0.3
S355J2+N	1.6	0.3
ARMCO	1.2	0.2
P355N	1.0	0.35

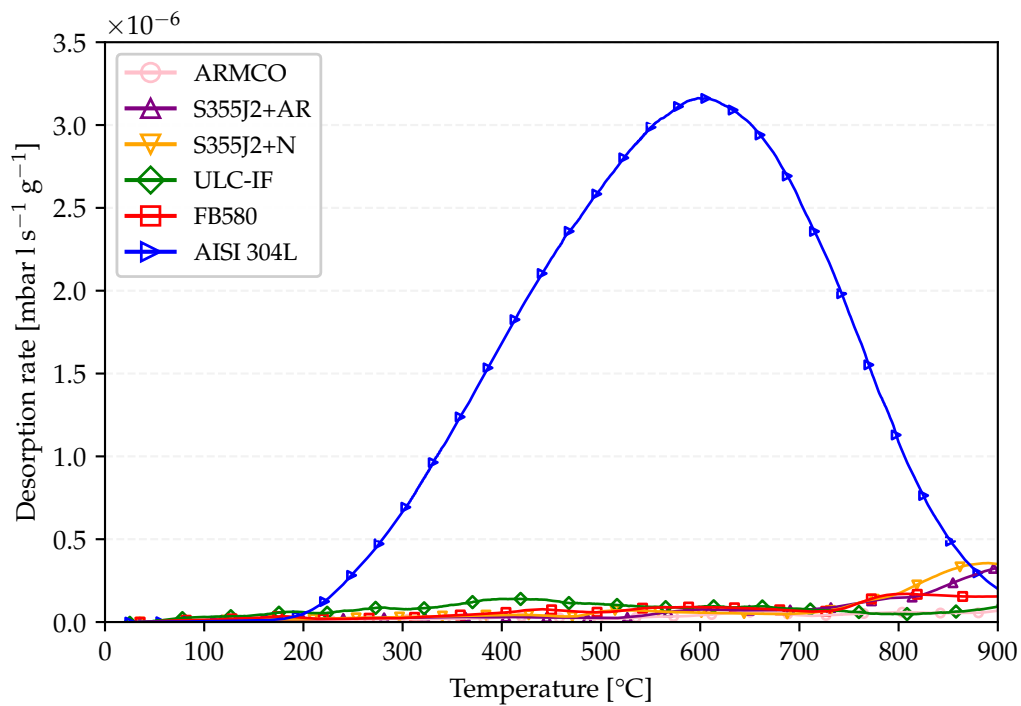


FIG. 17: H₂ thermal desorption spectra of AISI 304L and flat mild steel samples. The background signal of the TPD system is removed.

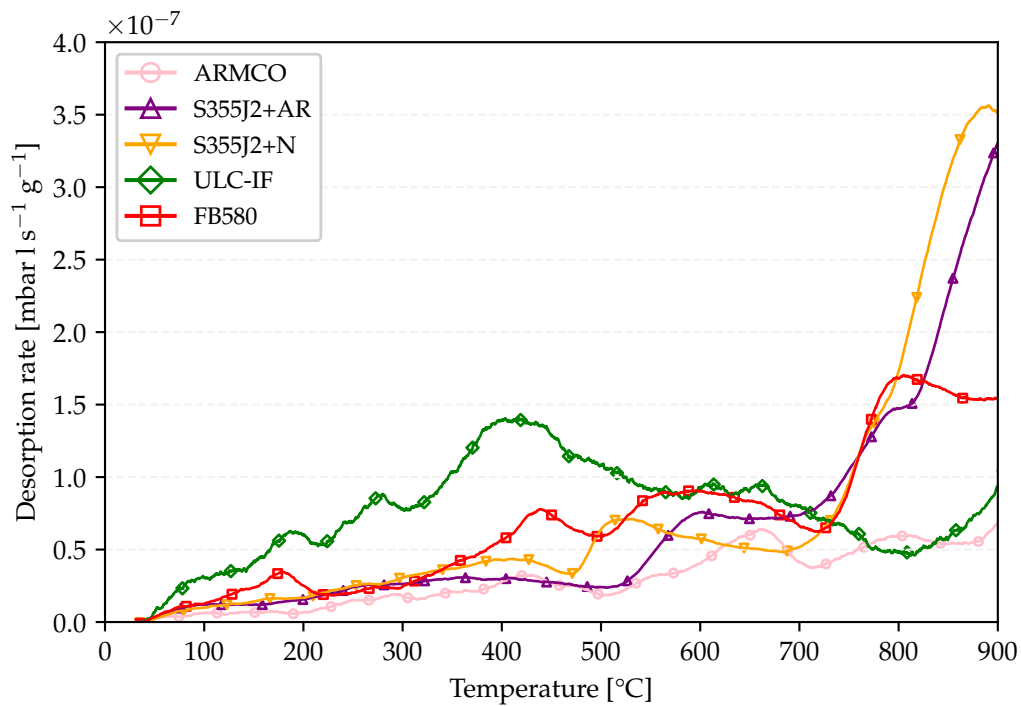


FIG. 18: H₂ thermal desorption spectra of flat mild steel samples (vertical scale reduced x10 with respect to Fig. 17). The background signal of the TPD system is removed.

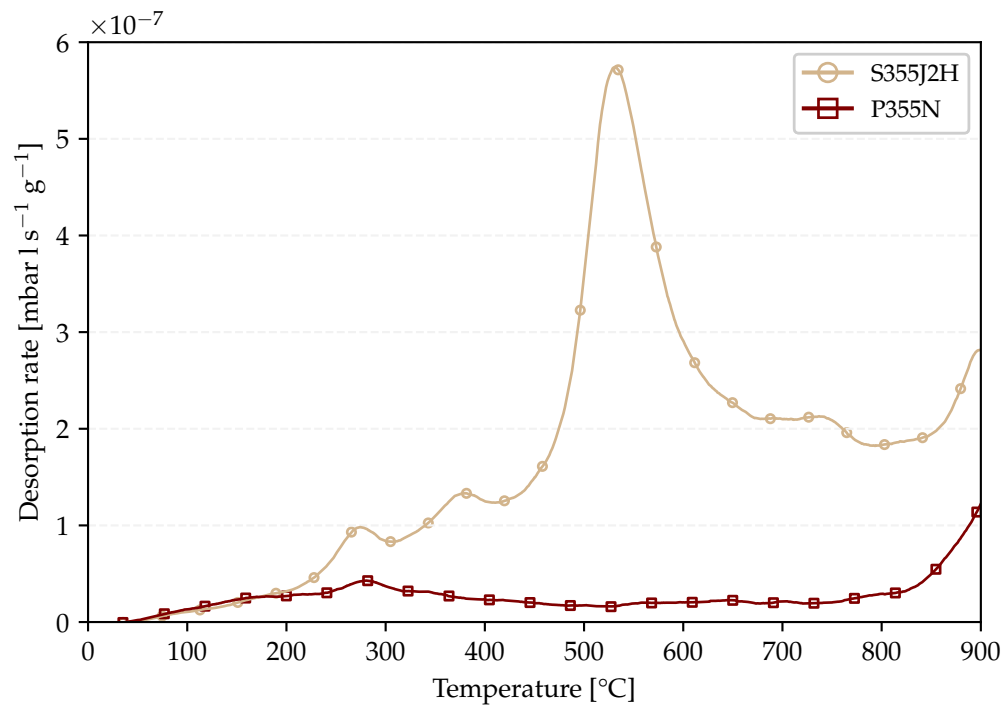


FIG. 19: H₂ thermal desorption spectra of mild steel samples from tubes. The background signal of the TPD system is removed.

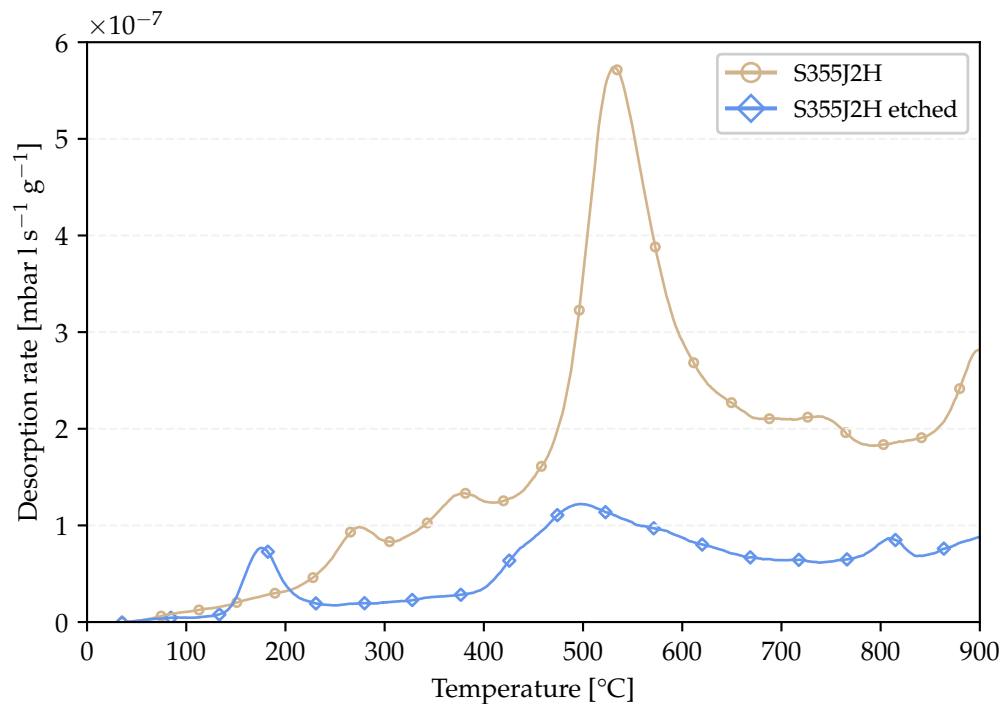


FIG. 20: H₂ thermal desorption spectra of S355J2H as received and after etching in a HCl solution. The background signal of the TPD system is removed.

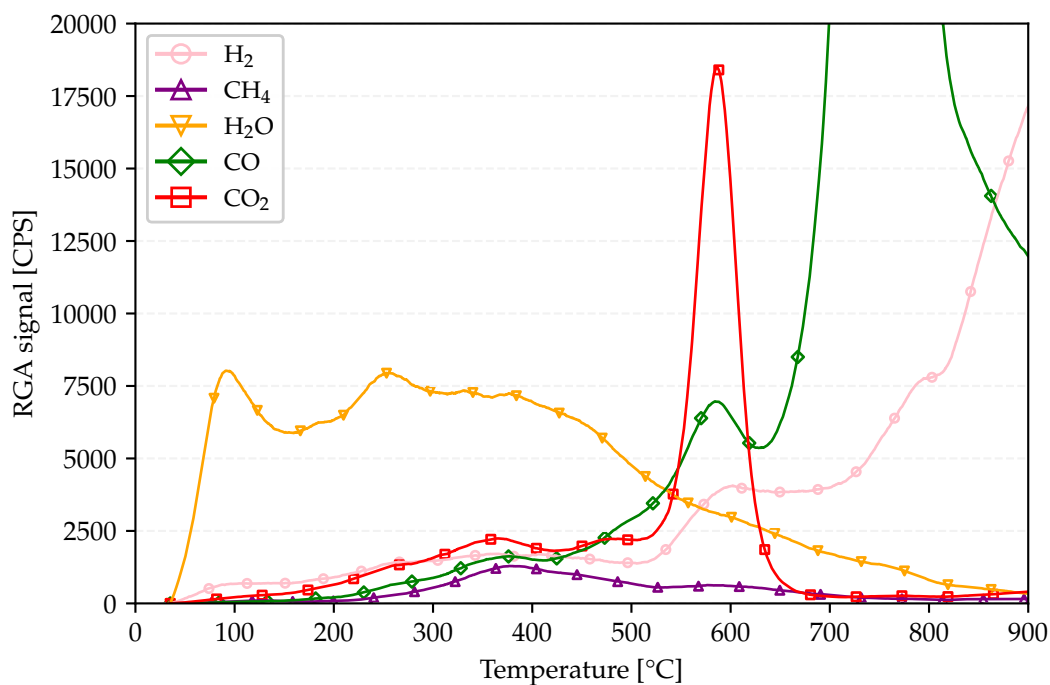


FIG. 21: Thermal desorption spectra of a S355J2+AR sample. The background signal of the TPD system is removed.

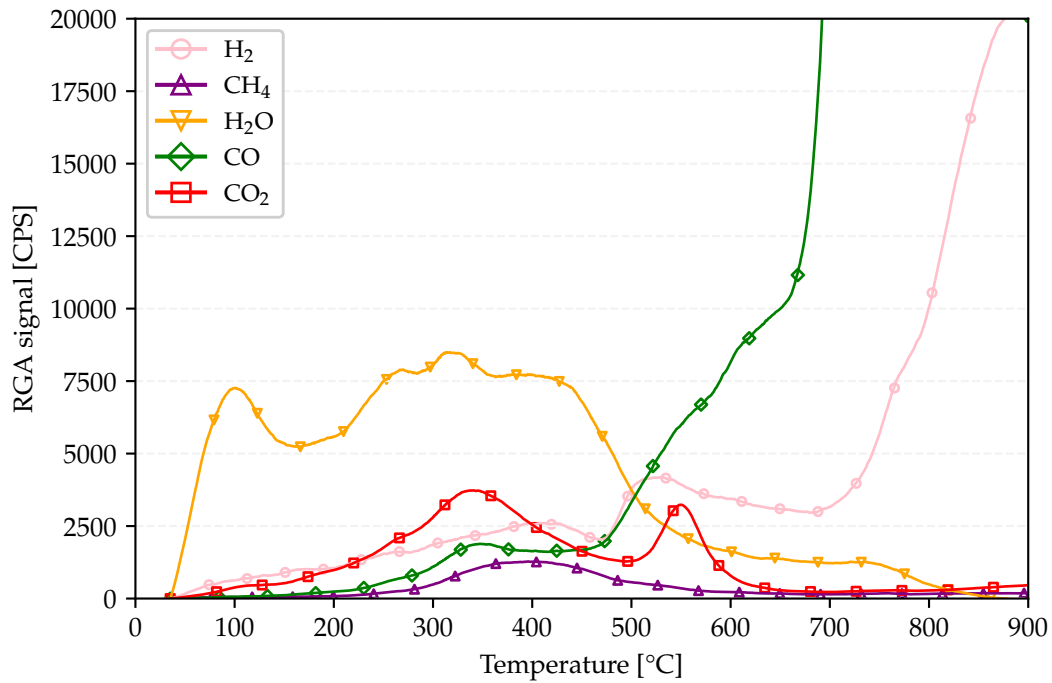


FIG. 22: Thermal desorption spectra of a S355J2+N sample. The background signal of the TPD system is removed.

D. OUTGASSING RATES AFTER BAKEOUT

The specific outgassing rates for H₂, CH₄, CO, and CO₂ are reported in Table IV and Table V. The values were calculated with Eq. (3) from data obtained by accumulation according to the procedure described in Section II B. The linearity of the pressure during the accumulation has been verified by measuring for different accumulation times.

As shown in Table IV, H₂ is the leading gas, with its outgassing rate being equal to or lower than 7.0×10^{-14} mbar l s⁻¹ cm⁻² after a 48 h bakeout at 80°C. A difference can be observed between the tubes and the flat sample, with the latter showing values below 6×10^{-15} mbar l s⁻¹ cm⁻². The measured specific outgassing rates of CH₄, CO and CO₂ range between 3×10^{-15} and 2×10^{-17} mbar l s⁻¹ cm⁻².

The following bakeout at 150°C for 48 hours (refer to Table 5 and Figure 16) yielded striking results. While the H₂ specific outgassing rate of the S355J2H tube remained constant at 1×10^{-14} mbar l s⁻¹ cm⁻², the S355J2+AR and P355N samples exhibited reductions by factors of 2.5 and 4, respectively. Additionally, for all other tested alloys, the total H₂ outgassing rate fell below the detection limit, defined as 50% of the background value. As per H₂, CO and CO₂ show an important outgassing rate reduction. CH₄ outgassing rates showed little to no decrease for most of the steel grades when the bakeout temperature was increased from 80°C to 150°C. The CO specific outgassing rate of the S355J2H tube could not be accurately determined due to a significant virtual leak originating from the sample itself. Fig. 27 illustrates that during the RGA measurement of accumulated gas, the increase in mass-28 signal correlates with rises in mass-14 and mass-40 signals, typical for N₂ and Ar. The mass-12 signal (C) could not be reliably used for calculating the CO contribution, as it may stem from fragmentation patterns of other gases like CH₄ and CO₂. Despite extensive leak detection efforts, no external leaks were found in the vacuum chamber or measuring system. The presence of virtual leaks suggests surface deterioration. Fig. 7 indicates porosities and cracks in the oxide layer likely responsible for an air in-leakage. The H₂ specific outgassing rates are qualitatively consistent with the hydrogen concentration measured by TPD. Compared with austenitic stainless steels, after bakeout at 150°C for 24 hours²¹, i.e 3×10^{-12} mbar l s⁻¹ cm⁻², the mild steel samples show from two to three orders of magnitude lower H₂ specific outgassing rates, therefore attaining values measured for a few mm thick AISI 304L after vacuum firing (950°C, 2 h)²¹ or air bakeout (390°C, 100 h)⁴¹. The hydrogen concentration ratios and the ratios of specific hydrogen outgassing rates in mild steels compared to austenitic steels don't align

quantitatively. This mismatch might be because hydrogen in mild steel is mainly trapped within the material's bulk and surface oxide, thus not participating in the diffusion process that causes outgassing at room temperature.

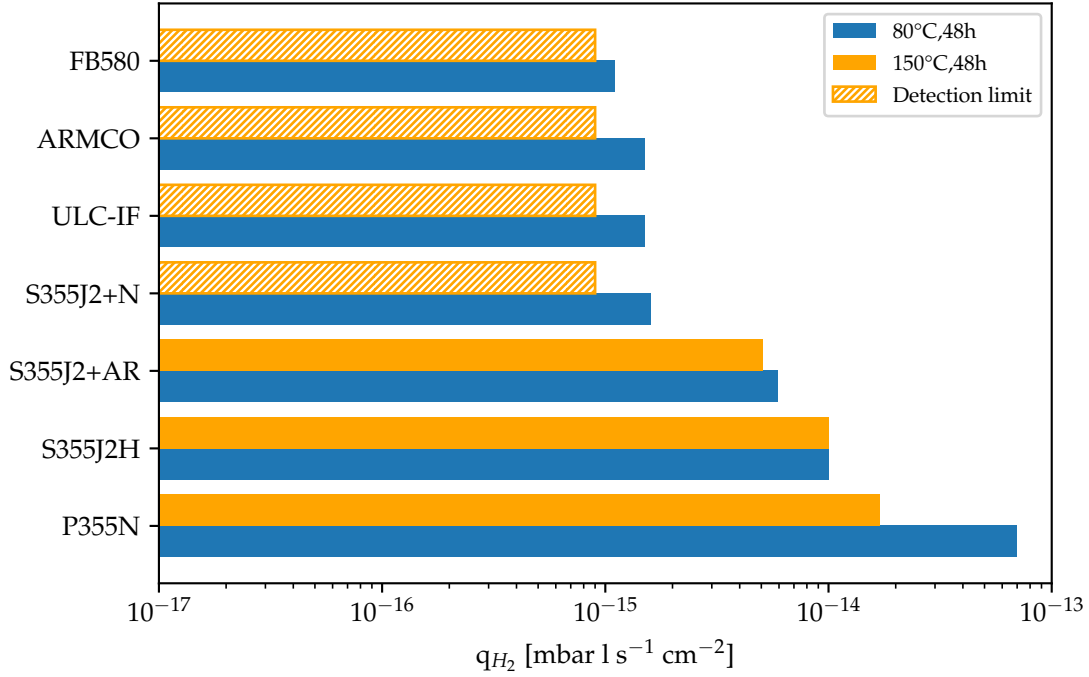


FIG. 23: Comparison of H₂ specific outgassing rate reported in Tables IV and V. The system sensitivity (see definition in the text) normalised to the sample surface area is plotted as orange-dashed columns when the measured values are below such a limit.

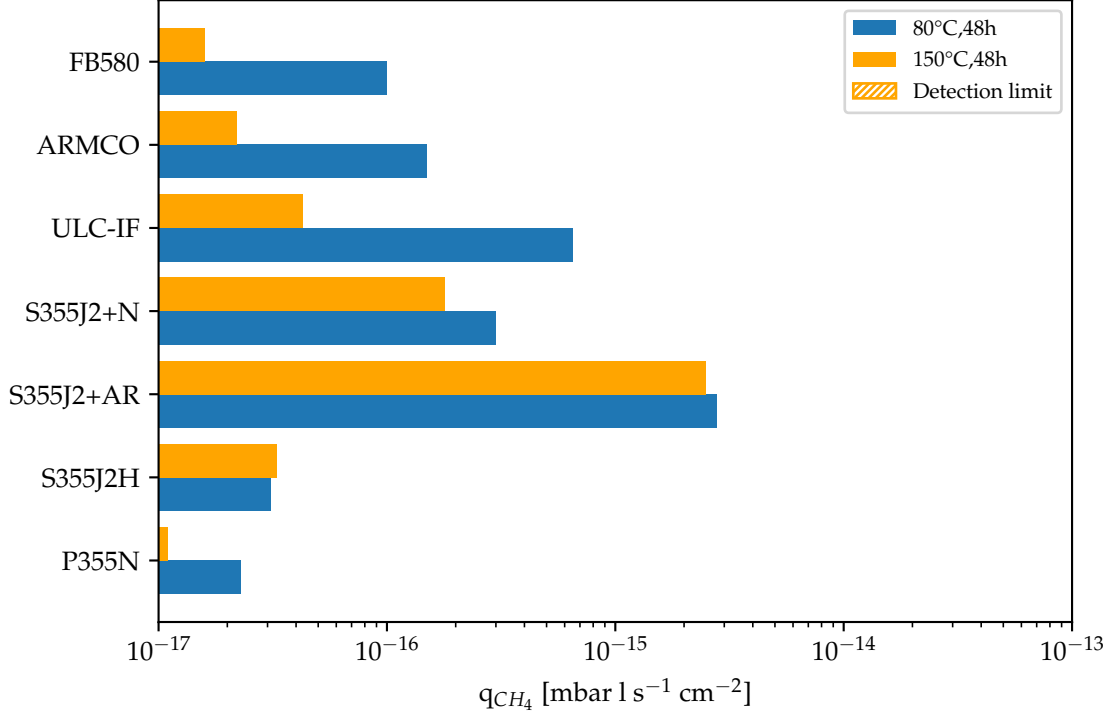


FIG. 24: Comparison of CH₄ specific outgassing rate reported in Table IV and Table V. The system sensitivity (see definition in the text) normalised to the sample surface area is plotted as an orange-dashed column when the measured values are below such a limit.

TABLE IV: Specific outgassing rates for the different steels at 21±2°C after bake-out at 80°C for 48 h. Background signal removed.

Steel grade	Specific outgassing rate [mbar l s ⁻¹ cm ⁻²]			
	H ₂	CH ₄	CO	CO ₂
P355N	7.0 × 10 ⁻¹⁴	2.3 × 10 ⁻¹⁷	8.0 × 10 ⁻¹⁶	1.0 × 10 ⁻¹⁶
S355J2H	1.0 × 10 ⁻¹⁴	3.1 × 10 ⁻¹⁷	N/A	3.4 × 10 ⁻¹⁶
S355J2+AR	5.9 × 10 ⁻¹⁵	2.8 × 10 ⁻¹⁵	3.6 × 10 ⁻¹⁵	1.1 × 10 ⁻¹⁵
S355J2+N	1.6 × 10 ⁻¹⁵	3.0 × 10 ⁻¹⁶	1.8 × 10 ⁻¹⁵	9.7 × 10 ⁻¹⁶
ULC-IF	1.5 × 10 ⁻¹⁵	6.5 × 10 ⁻¹⁶	7.4 × 10 ⁻¹⁶	2.3 × 10 ⁻¹⁶
ARMCO	1.5 × 10 ⁻¹⁵	1.5 × 10 ⁻¹⁶	2.8 × 10 ⁻¹⁵	6.5 × 10 ⁻¹⁵
FB580	1.1 × 10 ⁻¹⁵	1.0 × 10 ⁻¹⁶	2.3 × 10 ⁻¹⁶	8.5 × 10 ⁻¹⁶

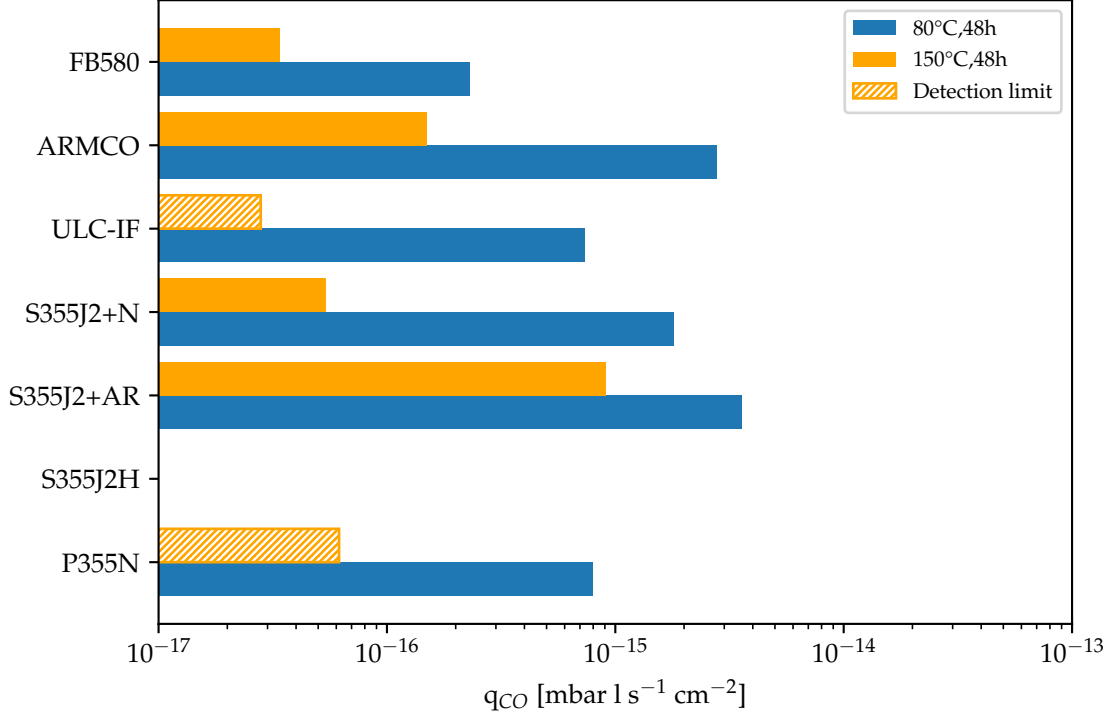


FIG. 25: Comparison of CO specific outgassing rate reported in Table IV and Table V. The system sensitivity (see definition in the text) normalised to the sample surface area is plotted as an orange-dashed column when the measured values are below such a limit. The lack of the data for S355J2H is explained in the text.

TABLE V: Specific outgassing rates for the different steels at $21 \pm 2^\circ\text{C}$ after bake-out at 150°C for 48h. Background signal removed. BSS: Below system sensitivity.

Steel grade	Specific outgassing rate [mbar l s ⁻¹ cm ⁻²]			
	H ₂	CH ₄	CO	CO ₂
P355N	1.7×10^{-14}	BSS	BSS	BSS
S355J2H	1.0×10^{-14}	3.3×10^{-17}	N/A	BSS
S355J2+AR	2.2×10^{-15}	2.5×10^{-15}	9.1×10^{-16}	2.9×10^{-16}
S355J2+N	BSS	1.8×10^{-16}	5.4×10^{-17}	BSS
ULC-IF	BSS	4.3×10^{-17}	BSS	BSS
ARMCO	BSS	2.2×10^{-17}	1.5×10^{-16}	BSS
FB580	BSS	1.6×10^{-17}	3.4×10^{-17}	BSS

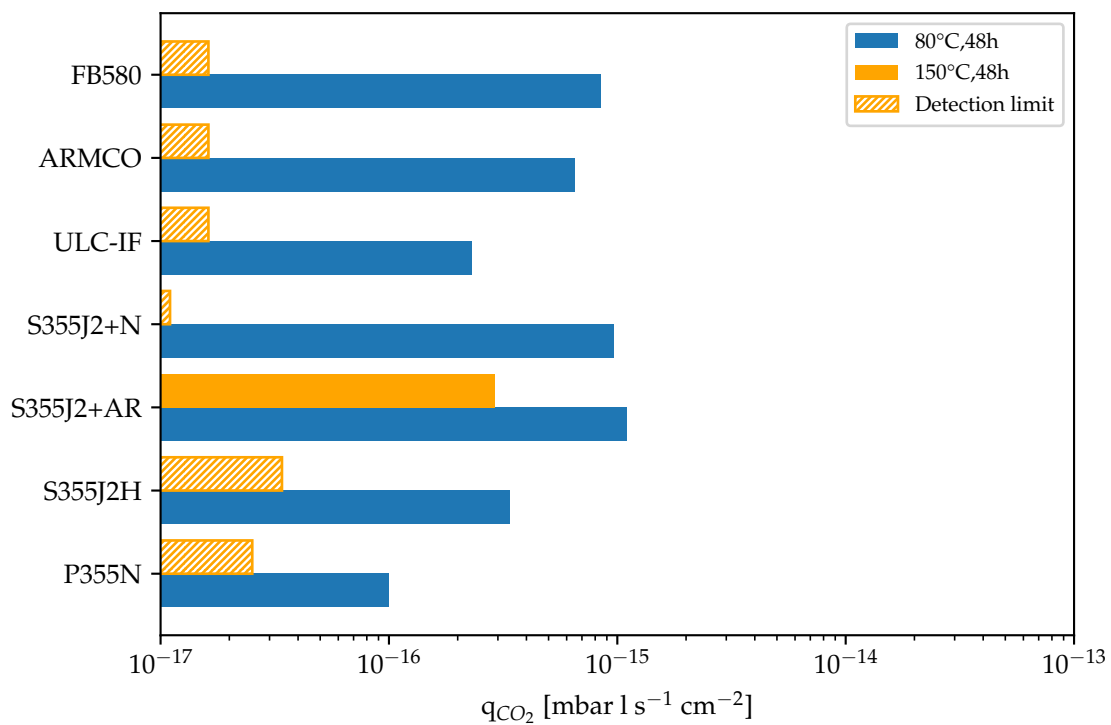


FIG. 26: Comparison of CO₂ specific outgassing rate reported in Table IV and Table V. The system sensitivity (see definition in the text) normalised to the sample surface area is plotted as orange-dashed columns when the measured values are below such a limit.

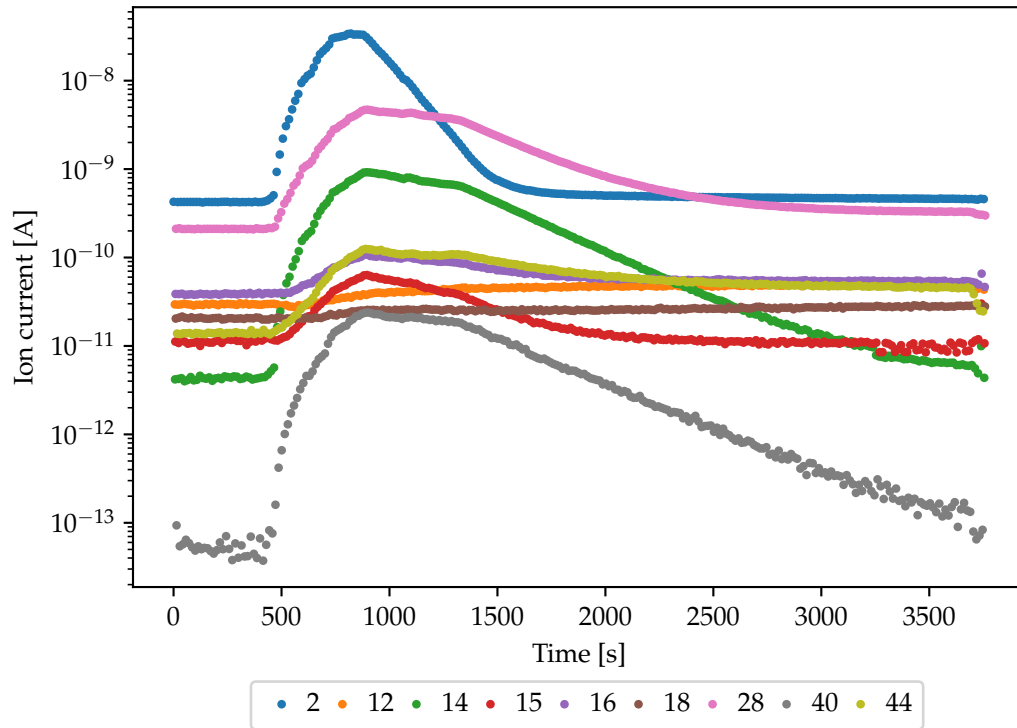


FIG. 27: MID scan of the accumulated gas in a S355J2H tube after 80°C, 48 h bake-out.

V. ULTIMATE PRESSURE AFTER LOW-TEMPERATURE BAKEOUT

The ultimate pressure measurements were performed on a P355N vacuum chamber (6.3 cm inner diameter, 320 cm long, 6333 cm² internal surface area). The results, with the background signal removed (equal to 1.5×10^{-11} mbar N₂ eq.) and expressed in N₂ equivalent, are reported in Fig. 28.

The P355N chamber, subjected to a series of consecutive heating steps at 80°C, each lasting 48 h, consistently exhibited a halving of total pressure between each heating step. Based on the results of the initial cycle, it was decided to vent the P355N chamber to laboratory atmosphere conditions (temperature: 21±2°C, relative humidity of about 50%) for 24 h and proceed with a second cycle of bakeouts to observe if the same pressure reduction trend persisted.

As depicted in Fig. 28, following the initial heating step of the second cycle, the pressure was 2.4 times lower compared to that of the first cycle. The pressure reduction between steps in the second cycle closely resembled that of the first cycle. After completing four heating steps, the tube was again vented with air at room temperature for an additional 24 h before extending the measurement campaign to a third cycle. The ultimate pressure after the initial heating step between the second and third cycles did not exhibit the same decrease as observed in the first two cycles. However, the decay between the heating steps remained consistent with previous observations.

The system was not equipped with an RGA to prevent undue contributions to the background signal, making it impossible to assess the gas species contributing to the total pressure directly. Nonetheless, valuable insights can be obtained from the specific outgassing rates measured using the coupled method for identical materials from the same production batch and subjected to identical cleaning procedures. For such materials, H₂ emerges as the dominant accumulated gas, while the contributions of CH₄, CO, and CO₂ are at least 87 times lower (see Table IV). Assuming the same specific H₂ outgassing rate for the P355N vacuum chamber under examination, the N₂ equivalent pressure contribution would be 6.5×10^{-12} mbar. Considering that the difference between the measured pressure and the H₂ contribution is approximately one order of magnitude, the measured pressure can primarily be attributed to water vapor, considering that its outgassing rate cannot be determined by accumulation methods, as noted previously.

After the three cycles, i.e. in total 12 bakeouts at 80°C for 48 h, the specific H₂ outgassing rate of the P355N vacuum chamber was directly measured by the coupled method following an additional bakeout at 80°C for 48 h. The measured value was 7.5×10^{-16} mbar l s⁻¹ cm⁻², nearly two

orders of magnitude lower than the value of Table IV, which was obtained after a single bakeout step at 80°C.

Once the outgassing measurement was completed, the P355N vacuum chamber was disconnected from the accumulation system and stored in air on a laboratory's shelf for 6 months, protected only by plastic caps at the extremities. Afterwards, the same chamber was reinstalled again on the ultimate pressure system, and it underwent a fourth cycle of bakeouts. The objective of the measurement was to test the effect of the storage in air on the ultimate pressure with respect to the values recorded in the previous three cycles.

After the initial bakeout of the fourth cycle, the ultimate pressure matches that of the second cycle (see Fig. 29). Subsequently, a reduction by a factor of three is achieved after an additional bakeout, and a third bakeout results in an ultimate pressure comparable to the latest one measured six months before exposure to air. The observed behaviours and trends across cycles can be attributed to surface modifications resulting from repeated bakeouts at 80°C. The conditioning effect appears permanent within the specified time frame of air exposure, opening the way for further investigations.

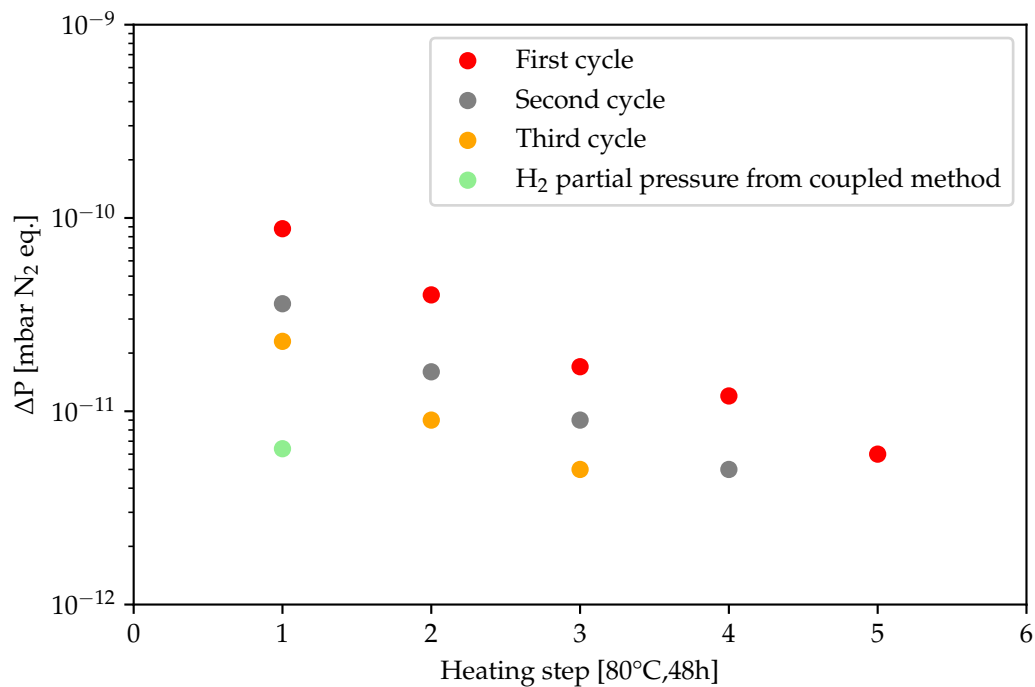


FIG. 28: Ultimate pressure measurements at 21°C. Background removed. The number of cycles has been reduced progressively with heating cycles given the measured values being too close to the background one and thus not allowing the calculation of a significant value. The calculated H₂ partial pressure resulting from accumulation measurements is also shown at the first heating step.

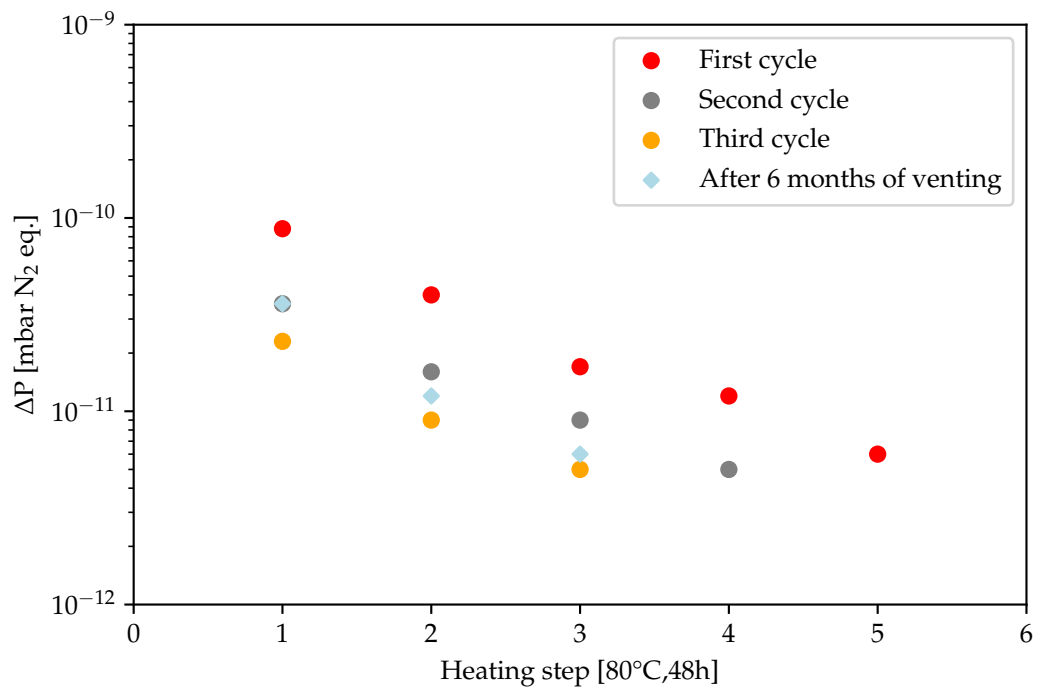


FIG. 29: Ultimate pressure measurements at 21°C including a fourth cycle obtained after a 6-month exposure in air. Background removed.

VI. CONCLUSIONS

In this work, we explored the UHV compatibility of mild steels and their applicability as structural materials for vacuum tubes of next-generation GWD.

For the selected samples, before bakeout, the water vapour outgassing rate follows the usual reciprocal function of the pumping time, while the values are from 1.3 to 9 times higher than those typically measured for ordinary austenitic stainless steel. These differences and large spans could be ascribed to the morphology of the surface oxide layers, whose thickness can range from 1 nm to 10 μm as highlighted by SEM/FIB cross-sectional analysis.

The hydrogen content in mild-steel samples, analysed by TPD up to 850°C, is significantly lower—ranging from 10 to 75 times less—than the levels typically observed in AISI 304L. This disparity was anticipated due to the lower hydrogen solubility inherent in body-centred cubic crystallographic structures, which are characteristic of mild steel. The TPD peaks indicate a more intricate desorption process than the typical behaviour seen in austenitic stainless steels, where hydrogen diffusion emerges as the dominant factor. The shape and positioning of these desorption peaks and the simultaneous release of carbon-containing molecules suggest that hydrogen liberation may be linked to de-trapping from the metal or the oxide layer. Structural transformations enhance the former, while chemical changes in the topmost layer may influence the latter. Notably, XPS detects alterations in the chemical composition of the oxide layer after just an 80°C bakeout. Although the investigation into the exact origin of these peaks falls beyond the scope of this study, given their significant impact on outgassing rates, they will be subject to further examination in subsequent research.

The bakeout temperatures chosen for this study are relatively low compared to the typical values used for UHV systems. This decision stems from the most practical and efficient method for baking the beampipe in GWD—utilizing the joule effect with electrical current applied to the vessel's walls. If the beampipes were constructed from mild steel in a pipeline-like design, the wall thickness would be approximately 1 cm thick, 2.5 to 3 times thicker than those currently utilized in GWD. Assuming the same insulation and bakeout temperature applied for LIGO and VIRGO (15 cm insulation and 150°C) and considering that the electrical resistivity of mild steels is 80% lower than that of 304L, the current to be applied is around 6000 A. It becomes apparent that bakeout would only be feasible at low temperatures, approximately around 80°C, where the current will drop to 4000 A, assuming the same conditions. This study demonstrates that such

low temperatures do not pose an issue for H₂ outgassing. Specifically, the measured H₂ specific outgassing rates, recorded at room temperature following a 48 h bakeout at 80°C, fall within the range of 10⁻¹⁴ mbar l s⁻¹ cm⁻², comparable to those observed in vacuum-fired or air-baked austenitic stainless steel vacuum chambers. These values align with the requirements for future gravitational wave detectors and provide the benefit of avoiding expensive and time-consuming high-temperature degassing treatments. However, the outgassing rate of water vapour remains a concern, as it predominantly influences the ultimate pressure after several days of bakeout at 80°C. Nevertheless, there is a gradual decrease in the ultimate pressure observed after a series of bakeouts at 80°C, indicating a progressive reduction in the outgassing rate of water vapour. This conditioning of the surface appears to be semi-permanent, lasting at least after half a year of exposure to air on a laboratory shelf. The nature of this behaviour and its implications for the feasibility of mild steel beampipes in GWD will be explored in further studies. It is also important to focus on developing surface quality, stability, and corrosion resistance to substantiate the feasibility of mild steel beampipes for the next generation of gravitational wave detectors.

ACKNOWLEDGMENTS

We thank Mr Rowan Hill-James and Dr Adrienn Baris for their contribution to the outgassing and metallurgical measurements, respectively.

This work has been sponsored by the Wolfgang Gentner Programme of the German Federal Ministry of Education and Research (grant no. 13E18CHA)

DATA AVAILABILITY

The data that support the findings of this study are available from the corresponding author upon reasonable request.

REFERENCES

- ¹B. P. Abbott *et al.* (LIGO Scientific Collaboration and Virgo Collaboration), “Observation of gravitational waves from a binary black hole merger,” *Phys. Rev. Lett.* **116**, 061102 (2016).
- ²D. V. Martynov *et al.*, “Sensitivity of the advanced ligo detectors at the beginning of gravitational wave astronomy,” *Phys. Rev. D* **93**, 112004 (2016).
- ³J. Aasi *et al.* (LIGO Scientific Collaboration), “Advanced ligo,” *Classical and Quantum Gravity* **32**, 074001 (2015).
- ⁴F. Acernese *et al.* (Virgo Collaboration), “Advanced virgo: a second-generation interferometric gravitational wave detector,” *Classical and Quantum Gravity* **32**, 024001 (2014).
- ⁵T. Akutsu *et al.* (KAGRA Collaboration), “Overview of KAGRA: Detector design and construction history,” *Progress of Theoretical and Experimental Physics* **2021**, 05A101 (2020).
- ⁶M. Evans *et al.*, “A horizon study for cosmic explorer: Science, observatories, and community,” (2021), arXiv:2109.09882 [astro-ph.IM].
- ⁷ET steering committee editorial team, “Einstein telescope design report update 2020,” (2020).
- ⁸P. Marin *et al.*, “Outgassing performances of an industrial prototype tube for the virgo antenna,” *Vacuum* **49**, 309–314 (1998).
- ⁹F. Dylla and others, “NSF Workshop on Large UHV Systems for Frontier Scientific Research,” (2019), LIGO-P1900072-v1.
- ¹⁰M. Wutz *et al.*, *Theory and practice of vacuum technology* (Fried, 1989).
- ¹¹K. Jousten, “Materials,” in *Handbook of Vacuum Technology* (John Wiley & Sons, Ltd, 2016) Chap. 16, pp. 747–776.
- ¹²M. Morcillo, D. de la Fuente, I. Díaz, and H. Cano, “Atmospheric corrosion of mild steel,” *Revista de Metalurgia* **47**, 426–444 (2011).
- ¹³W. Wheeler and M. Carlson, “Transaction of the 8th national vacuum symposium, 1961,” (1962).
- ¹⁴M. Hablanian, *High-Vacuum Technology: A Practical Guide, Second Edition (2nd ed.)* (Routledge, 1997).
- ¹⁵Y. Ishimori *et al.*, “Outgassing rates of stainless steel and mild steel after different pretreatments,” *SHINKU* **14**, 295–301 (1971).
- ¹⁶C. D. Park *et al.*, “Reduction in hydrogen outgassing from stainless steels by a medium-temperature heat treatment,” *Journal of Vacuum Science & Technology A* **26**, 1166–1171 (2008).

- ¹⁷C. Park *et al.*, “Thermal outgassing rates of low-carbon steels,” *Journal of Vacuum Science & Technology A* **34**, 021601 (2015).
- ¹⁸C. Park *et al.*, “Vacuum characteristic of a chamber made of mild steel,” *Applied Science and Convergence Technology* **24**, 84–89 (2015).
- ¹⁹J. Fedchack, “A review of recent outgassing studies on mild and stainless steels,” *Beampipes for Gravitational Wave Telescopes 2023, Workshop, CERN* (2023).
- ²⁰P. Redhead, J. Hobson, and E. Kornelsen, *The Physical Basis of Ultrahigh Vacuum*, High vacuum series (Chapman and Hall, 1968).
- ²¹P. Chiggiato, “Outgassing properties of vacuum materials for particle accelerators,” (2020), arXiv:2006.07124 [physics.acc-ph].
- ²²C. Benvenuti and M. Hauer, “Pressure measurements for the ISR at CERN; 1973 ed.” Tech. Rep. (CERN, Geneva, 1973).
- ²³C. Benvenuti *et al.*, “Pressure measurements for the ISR at CERN,” Tech. Rep. (CERN, Geneva, 1977).
- ²⁴Hidden Analytical, “TPD workstation,” .
- ²⁵R. Calder and G. Lewin, “Reduction of stainless-steel outgassing in ultra-high vacuum,” *British Journal of Applied Physics* **18**, 1459 (1967).
- ²⁶M. Malabaila and L. Ferreira, “Operating procedure for chemical degreasing of parts for high-vacuum and ultra-high-vacuum applications (EDMS n^o: 1390437 v.3),” Tech. Rep. (2022).
- ²⁷GS-IS & EN-MME, “Tech. spec. n^o1004 - 1.4306 - stainless steel sheets/plates for vacuum applications (EDMS n^o: 790767),” Tech. Rep. (2013).
- ²⁸H. F. Dylla *et al.*, “Correlation of outgassing of stainless steel and aluminum with various surface treatments,” *Journal of Vacuum Science & Technology A* **11**, 2623–2636 (1993), https://pubs.aip.org/avs/jva/article-pdf/11/5/2623/6036643/2623_1_online.pdf.
- ²⁹Edwards, D. Jr., “Upper bound to the pressure in an elementary vacuum system,” *Journal of Vacuum Science and Technology* **14**, 606–610 (1977), https://pubs.aip.org/avs/jvst/article-pdf/14/1/606/11939249/606_1_online.pdf.
- ³⁰M. C. Biesinger *et al.*, “Resolving surface chemical states in xps analysis of first row transition metals, oxides and hydroxides: Cr, mn, fe, co and ni,” *Applied Surface Science* **257**, 2717–2730 (2011).
- ³¹N. S. McIntyre and D. G. Zetaruk, “X-ray photoelectron spectroscopic studies of iron oxides,” *Analytical Chemistry* **49**, 1521–1529 (1977).

- ³²A. Savitzky and M. J. E. Golay, “Smoothing and differentiation of data by simplified least squares procedures.” *Analytical Chemistry* **36**, 1627–1639 (1964).
- ³³D. Grant *et al.*, “Hydrogen in 316 steel — diffusion, permeation and surface reaction,” *Journal of Nuclear Materials* **152**, 139–145 (1988).
- ³⁴A. N. Itakura *et al.*, “Model of local hydrogen permeability in stainless steel with two coexisting structures,” *Scientific Reports* **11**, 8553 (2021).
- ³⁵M. Louthan and R. Derrick, “Hydrogen transport in austenitic stainless steel,” *Corrosion Science* **15**, 565–577 (1975).
- ³⁶R. Oriani, “The diffusion and trapping of hydrogen in steel,” *Acta Metallurgica* **18**, 147–157 (1970).
- ³⁷K. Wilson and M. Baskes, “Deuterium trapping in irradiated 316 stainless steel,” *Journal of Nuclear Materials* **76-77**, 291–297 (1978).
- ³⁸K. Wilson and M. Baskes, “Deuterium re-emission from 304In stainless steel,” *Journal of Nuclear Materials* **111-112**, 622–627 (1982).
- ³⁹D. Wagner *et al.*, “A laboratory study of the reduction of iron oxides by hydrogen,” in *Sohn International Symposium*, Vol. vol. 2 “Thermo and physicochemical principles: iron and steel making”, edited by F. Kongoli and R. Reddy (TMS, San Diego, United States, 2006) pp. 111–120.
- ⁴⁰“Iron-Carbon Phase Diagrams,” in *Heat Treating of Irons and Steels* (ASM International, 2014) <https://dl.asminternational.org/handbooks/book/chapter-pdf/463142/a0005995.pdf>.
- ⁴¹M. Bernardini *et al.*, “Air bake-out to reduce hydrogen outgassing from stainless steel,” *Journal of Vacuum Science & Technology A* **16**, 188–193 (1998), https://pubs.aip.org/avs/jva/article-pdf/16/1/188/11013996/188_1_online.pdf.